

# Star formation in mergers with cosmologically motivated initial conditions

Wouter Karman<sup>1,2\*</sup>, Andrea V. Macciò<sup>2</sup>, Rahul Kannan<sup>2,3</sup>, Benjamin P. Moster<sup>4</sup>, Rachel S. Somerville<sup>5</sup>

<sup>1</sup> *Kapteyn Astronomical Institute, University of Groningen, Postbus 800, 9700 AV Groningen, the Netherlands*

<sup>2</sup> *Max-Planck-Institut für Astronomie, Königstuhl 17, 69117 Heidelberg, Germany*

<sup>3</sup> *Department of Physics, Kavli Institute for Astrophysics and Space Research, Massachusetts Institute of Technology, Cambridge, MA 02139, USA*

<sup>4</sup> *Kavli Institute for Cosmology, Institute of Astronomy, University of Cambridge, Madingley Road, Cambridge CB3 0HA, UK*

<sup>5</sup> *Department of Physics and Astronomy, Rutgers University, 136 Frelinghuysen Road, Piscataway, NJ 08854, USA*

8 July 2015

## ABSTRACT

We use semi-analytic models and cosmological merger trees to provide the initial conditions for multi-merger numerical hydrodynamic simulations, and exploit these simulations to explore the effect of galaxy interaction and merging on star formation (SF). We compute numerical realisations of twelve merger trees from  $z = 1.5$  to  $z = 0$ . We include the effects of the large hot gaseous halo around all galaxies, following recent observations and predictions of galaxy formation models. We find that including the hot gaseous halo has a number of important effects. Firstly, as expected, the star formation rate on long timescales is increased due to cooling of the hot halo and refuelling of the cold gas reservoir. Secondly, we find that interactions do not always increase the SF in the long term. This is partially due to the orbiting galaxies transferring gravitational energy to the hot gaseous haloes and raising their temperature. Finally we find that the relative size of the starburst, when including the hot halo, is much smaller than previous studies showed. Our simulations also show that the order and timing of interactions are important for the evolution of a galaxy. When multiple galaxies interact at the same time, the SF enhancement is less than when galaxies interact in series. All these effects show the importance of including hot gas and cosmologically motivated merger trees in galaxy evolution models.

**Key words:** galaxies: active, evolution, interactions, starburst, star formation – methods: numerical

## 1 INTRODUCTION

In the now well established model of Lambda Cold Dark Matter ( $\Lambda$ CDM) mergers and interactions between galaxies play an important role in shaping their evolution (e.g. White & Rees 1978). Both observations and theoretical studies have shown that interactions between galaxies can create tidal bridges, streams and shells (e.g. Zwicky 1956; Toomre & Toomre 1972; Toomre 1977; Smith et al. 2007). Minor mergers have been shown to thicken disks and build up the spheroidal component (Quinn et al. 1993; Walker et al. 1996; Villalobos & Helmi 2008, 2009; Moster et al. 2010, 2012; Zolotov et al. 2010), while major mergers have been shown to destroy disks and create elliptical and bulge dominated galaxies (Hernquist

1992; Quinn et al. 1993; Brook et al. 2004; Cox et al. 2006; Kazantzidis et al. 2008, 2009, but see Robertson et al. 2006; Governato et al. 2009; Querejeta et al. 2015 for disks surviving major mergers).

Mergers and interactions are very common — over 70% of Milky Way-sized galaxies have experienced a 10:1 merger since redshift  $z \sim 1$  (Stewart et al. (2008); Lotz et al. (2011, e.g.)). Furthermore, a significant amount of the mass formed in galaxies has been assembled by accreting smaller galaxies, varying from 10 % to >50% of the stellar mass for galaxies with  $M_\star > 10^{10} M_\odot$  (e.g. Oser et al. 2010; Lackner et al. 2012; Navarro-González et al. 2013). Bell et al. (2006) used pairs at the same redshift in the COMBO-17 photometric redshift survey to study the rate of interactions between galaxies. They found that in their sample  $\sim 5\%$  of the galaxies are in a close pair. They also found that 50% of the massive galaxies have undergone a major merger since  $z = 0.8$ ,

\* karman@astro.rug.nl

and therefore conclude that major mergers play a significant role in the evolution of galaxies in this period.

An important effect of galaxy interactions and mergers is that they cause enhanced star formation (SF) (Larson & Tinsley 1978; Barton Gillespie et al. 2003; Lin et al. 2007; Hwang et al. 2011; Patton et al. 2011), although weak in the local Universe (Bergvall et al. 2003; Knapen & James 2009), and may trigger AGN activity (e.g. Sanders et al. 1988; Treister et al. 2012; Bessiere et al. 2014). There is increasing evidence that most extreme local star forming galaxies, the Ultra Luminous InfraRed Galaxies (ULIRGS), are triggered by mergers (e.g. Sanders & Mirabel 1996; Borne et al. 1999, 2000; Bushouse et al. 2002; Rupke & Veilleux 2013), and an anti-correlation is found between galaxy pair separation and the indicators for SF in the optical (e.g. equivalent width of  $H\alpha$ , Sanders et al. 1988; Barton et al. 2000; Nikolic et al. 2004; Ellison et al. 2008; Patton et al. 2011).

Galaxy mergers have been studied extensively using idealised binary merger simulations (e.g. Toomre 1977; Hernquist 1992; Mihos & Hernquist 1996; Springel et al. 2005; Cox et al. 2008; Hopkins et al. 2009). In this approach, two idealised (typically disk-dominated) galaxy models are created, each within their own idealised dark matter halo, and these are set up on an orbit which will lead to an eventual merger. The evolution during the course of the merger is then computed using numerical N-body and hydrodynamic techniques. These studies predict a strong link between galaxy interactions and enhanced star formation. During interactions, the gravitational potential is disturbed, such that gas is able to lose angular momentum and flow inwards. Because of this, the gas density in the center increases rapidly, and a burst of SF (starburst) takes place in the center of the galaxy (Mihos & Hernquist 1996; Springel et al. 2005; Cox et al. 2008). Cox et al. (2008) and Hopkins et al. (2009) quantified this increased SF due to galaxy interaction and found that it is proportional to the mass ratio of the merging galaxies, as well as their cold gas fraction before the onset of the merger. Many semi-analytic models use the fitting formulae derived from these studies to model merger-driven starbursts (e.g. Bower et al. 2006; Croton et al. 2006; De Lucia & Blaizot 2007; Monaco et al. 2007; Somerville et al. 2008).

The majority of these previous idealised merger simulations include a cold gaseous disk in the galaxy model, but did not consider the hot gas component harboured in the dark matter halo. Full cosmological hydrodynamical simulations and semi-analytic models (SAMs) of galaxy formation predict a large amount of hot gas around the galaxy, in quasi static equilibrium with the gravitational potential (e.g. Kauffmann et al. 1993; Bower et al. 2006; Somerville et al. 2008; Stinson et al. 2010, 2012; Brook et al. 2014, but see also Cox et al. 2004 for the generation of a hot halo during mergers). Recently, several X-ray studies found evidence for a hot gas component around the Milky Way (Gupta et al. 2012; Hodges-Kluck & Bregman 2013) and normal massive disc galaxies (e.g. Anderson & Bregman 2011; Anderson et al. 2013) with temperatures of more than  $10^5$  K.

This hot gas component was first included in idealised hydrodynamical merger simulations by Kim et al. (2009) and Moster et al. (2011). The latter found that the cool-

ing of the hot gaseous halo refuels the cold gas in the center of galaxies, and as a result, SF can be sustained for a longer time (see also Choi et al. 2014). Another interesting result of Moster et al. (2011) is that the efficiency of mergers in triggering SF is reduced in the presence of a hot halo.

An additional drawback of the idealised binary merger approach is that initial conditions (such as the properties of the progenitor galaxies and the orbit) must be specified *a priori*, and will not necessarily represent a cosmologically motivated distribution. In addition, such studies have been almost entirely restricted to binary mergers, while *multiple mergers* (a sequence of more than two mergers, in which the remnant does not have time to fully relax before a subsequent merger) are a common phenomenon in the CDM universe (e.g. Väisänen et al. 2008; Duplancic et al. 2013, MMS14).

In this paper we take advantage of the method developed by Moster et al. (2014), which combines cosmological merger trees and semi-analytic models to specify well-motivated, cosmologically representative initial conditions for a set of galaxy mergers, and then carries out the evolution of the galaxies in the merger tree using detailed numerical hydrodynamics. This approach is complementary to fully cosmological hydrodynamic “zoom-in” simulations, in that very high resolution can be achieved, and controlled experiments to study specific physical processes can be carried out. This is particularly relevant for testing and refining recipes for use in semi-analytic models. We extend the work of Moster et al. (2014) by including the effect of supermassive black holes (BHs) and their associated feedback in our merger simulations and studying the modifications to the star formation rate (SFR) during mergers with respect to models without BHs.

The paper is organised as follows: in Sec. 2 we describe the methods that we employed in this work, including the code that has been used, the physical recipes that we adopted and the models that were used to create the initial conditions. In Sec. 3 to 4 we present our results. We first compare simulations with and without the hot halo component in Sec. 3, then we inspect the effect of multiple mergers in Sec. 4, and finally we present the effects of BHs in the simulations in Sec. 5. We discuss the performance of the code and possible shortcomings of the models in Sec. 6, and then present our conclusions from this study and possible improvements for future studies in Sec. 7.

## 2 METHODS

In this section we briefly describe the modelling approach used in this paper, which is based on the simulated merger tree method described in detail in MMS14. The method consists of three main steps: 1) merger trees are extracted from a large dissipationless cosmological N-body simulation 2) a semi-analytic model is run in these merger trees to “populate” the halos with galaxies and predict their properties 3) each time two (or more) dark matter halos merge, galaxy-halo models are created with properties predicted by the SAM, placed on orbits specified by the cosmological simulation, and evolved forward using a numerical hydrodynamic code. More details about each of the three aspects are given below.

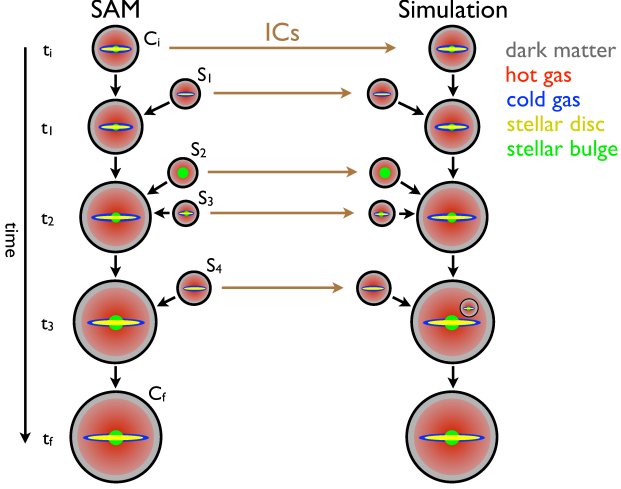


**Figure 1.** Schematic view of the scheme to combine SAMs and merger simulations (Fig. 6 from MMS14). On the left side the semi-analytic merger tree is shown with time running from top to bottom. At the starting time  $t_i$ , a particle realisation of the central galaxy is created using the properties of the central galaxy in the SAM at this time. This system is then simulated with the hydrodynamical code until the time of the first merger  $t_1$ , where a particle realisation of the first satellite  $S_1$  galaxy is created, again using the properties predicted by the SAM, and introduced into the simulation with orbit properties taken from the cosmological  $N$ -body simulation. The resulting merger is simulated until the next galaxies ( $S_2$  and  $S_3$ ) enter the main halo at  $t_2$ , at which point they are also included in the simulation. This procedure is repeated for all mergers until the final time of the run  $t_f$ .

## 2.1 Cosmological N-body simulation

The initial  $N$ -body simulation from which we extracted the merger trees was performed with the GADGET2 code (Springel 2005) assuming WMAP3 cosmological parameters (Spergel et al. 2007) namely:  $\Omega_m = 0.26$ ,  $\Omega_\Lambda = 0.74$ ,  $h = H_0/(100 \text{ km s}^{-1} \text{ Mpc}^{-1}) = 0.72$ ,  $\sigma_8 = 0.77$  and  $n = 0.95$ . The simulation was done in a periodic box with a side length of 100 Mpc, and contains  $512^3$  particles with a particle mass of  $2.8 \times 10^8 M_\odot$  and a comoving force softening of 3.5 kpc. Dark matter haloes were identified in the simulation snapshots using a Friends of Friends (FOF) halo finder with a linking parameter of  $b = 0.2$ . Substructures inside the FOF groups are then identified using the SUBFIND code (Springel et al. 2001).

## 2.2 Hydrodynamical simulations

The hydrodynamical simulations in this work were performed using the parallel TREE-SPH code PGADGET3 last described by Springel (2005). This code uses Smoothed Particle Hydrodynamics (SPH; Lucy 1977; Gingold & Monaghan 1977; Monaghan 1992) to evolve the gaseous medium using an entropy conserving scheme (Springel & Hernquist 2002).

Important parameters in SPH simulations are the softening length and the number of particles used. For the softening length  $\epsilon$  we follow MMS14 and for every particles species we set it to  $\epsilon = \epsilon_1 \sqrt{m_{\text{part}}/10^{10} M_\odot}$  (Dehnen 2001), where  $\epsilon_1 = 32 \text{ kpc}$  for a particle of  $10^{10} M_\odot$ . For one of our

typical simulations, the number of particles are  $\sim 800000$  DM particles,  $\sim 600000$  gas particles, and  $\sim 60000$  star particles, with masses of  $\sim 4 \times 10^5 M_\odot$ ,  $\sim 3 \times 10^6 M_\odot$ , and  $\sim 2 \times 10^5 M_\odot$  respectively. In Table A1 we give the number of particles for the major components in our merger trees.

The multiphase interstellar medium is modelled following the SF recipe introduced by Springel & Hernquist (2003). This subgrid recipe stochastically forms stars when cold gas clouds surpass a density threshold ( $\rho_{\text{th}}$ ). The newly formed stars eject a fraction of their material, modelling Supernova (SN) driven winds, following Springel & Hernquist (2003). The star formation is thus directly coupled to SN feedback on a subgrid level, such that the wind mass is directly proportional to the SFR, i.e.  $\dot{M}_w = \eta \dot{M}_*$ , where  $\eta$  is the mass loading factor which quantifies the wind efficiency. These gas particles receive a fixed fraction of the SN energy and are decoupled from hydrodynamical interactions for a short period of time, resulting in a constant initial wind speed  $v_w$ .

The parameters for the multiphase ISM model are computed as outlined in Springel & Hernquist (2003) in order to match the Kennicutt-Schmidt Law (Kennicutt 1998). When a Kroupa IMF is adopted, the mass fraction of massive stars is  $\beta = 0.16$  resulting in a cloud evaporation parameter of  $A_0 = 1250$  and a SN “temperature” of  $T_{\text{SN}} = 1.25 \times 10^8 \text{ K}$ . The SF timescale is set to  $t_*^0 = 3.5 \text{ Gyr}$  and for the galactic winds we adopt a mass-loading factor of  $\eta = 1$  and a wind speed of  $v_w \sim 500 \text{ km s}^{-1}$ , which is an intermediate strength for winds.

Every simulation is repeated with BHs included and thermal AGN feedback implemented as described by Springel et al. (2005). BH particles accrete mass by Eddington limited Bondi-Hoyle accretion (Hoyle & Lyttleton 1939; Bondi & Hoyle 1944; Bondi 1952), and this accretion is assumed to deposit thermal energy into the surrounding medium at a rate proportional to the accretion rate:  $\dot{E}_{\text{feed}} = \epsilon_f \epsilon_r \dot{M}_{\text{BH}} c^2$  where  $\epsilon_f$  is the coupling strength of the feedback, and is adopted from Di Matteo et al. (2005), and  $\epsilon_r$  is the standard conversion factor of rest-mass to energy for a standard thin accretion disk from Shakura & Sunyaev (1973).

When galaxies merge, their BH are both brought to the center of the remnant. During this migration, AGN offset from the center and pairs of AGN are predicted in the remnant. Observations have shown that off-set and dual AGN are present in a fraction of merging galaxies (e.g. Comerford et al. 2009; Koss et al. 2012; Comerford & Greene 2014). Because the movement and orbit of a second BH in galaxy mergers can be important for the evolution of the remnant, we do not reposition the BH particles on the local minimum of the potential. On the other hand we need to have stable BH particles, whose position is not affected by the finite resolution of the simulation (for example due to two body encounters with massive star particles).

In order to overcome this problem we defined a new parameter named *SeedRatio* (SR), which defines the initial ratio between the seed BH mass (i.e. the actual BH mass) and its dynamical mass. The dynamical mass is only used by the gravitational computations; by increasing it with respect to the actual BH mass we ensure that two body encounters between star (or gas) particles and the BH will not sub-

**Table 1.** Summary of the parameters used for the simulations of merger trees and their fiducial values.

Parameter	Description	Fiducial value
$z_i$	Redshift at the start of the simulation	1.5
$\mu_{\min}$	Minimum dark-matter mass ratio	0.0667/0.02
$\zeta$	Ratio of scaleheight and scalelength of the stellar disc	0.15
$\chi$	Ratio of scalelengths between gaseous and stellar disc	1.5
$\xi$	Ratio of gaseous halo core radius and dark matter halo scale radius	0.22
$\beta_{\text{bg}}$	Slope parameter of gaseous halo	0.67
$\alpha$	Ratio of specific angular momentum between gaseous and dark halo	4.0
$N_*$	Expected final number of stellar particles in the central galaxy	200 000
$\kappa$	Ratio of dark matter and stellar particle mass	15.0
$N_{\text{res,sat}}$	Ratio of satellite and central galaxy particle mass	1.0
$N_{\min}$	Minimum number of particles in one component	100
$\epsilon_1$	Softening length in kpc for particle of mass $m = 10^{10} M_{\odot}$	32.0
$t_0^*$	Gas consumption time-scale in Gyr for SF model	3.5 <sup>†</sup>
$A_0$	Cloud evaporation parameter for SF model	1250.0 <sup>†</sup>
$\beta_{\text{SF}}$	Mass fraction of massive stars for SF model	0.16 <sup>†</sup>
$T_{\text{SN}}$	Effective supernova temperature in K for feedback model	$1.25 \times 10^8$ <sup>†</sup>
$\eta$	Mass loading factor for wind model	1.0
$v_{\text{wind}}$	Initial wind velocity in $\text{km s}^{-1}$ for wind model	500.0
<i>SeedRatio</i>	Ratio of seed mass and dynamical mass of BH particle	0.01

<sup>†</sup> The SF parameters assume a Kroupa IMF.

stantially modify the BH trajectory. On the other hand all physical processes associated with the BH (e.g. feedback) are governed by its real mass and are not influenced by our choice of the initial SR ratio.

It should be noted that as the BH gradually accretes mass at a subgrid level, only the actual mass of the BH increases, while when another particle is swallowed by the BH particle the dynamical mass increases. We found that a ratio of 1000 for dynamical masses of BH particles to gas particles ensures very stable BHs orbits in all our merger simulations. At our resolution this results in  $SR = 0.01$  (meaning the BH dynamical mass is 100 times the BH mass). An overview of parameter values used in this work is given in Table 1.

Before moving to the next section, we would like to comment on the possible effects of the shortcomings of the PGADGET3 implementation of the SPH method on our results. Recently, Hayward et al. (2014) showed that the agreement between the adaptive mesh refinement (AMR) approach and SPH methods is very good with regard to SFRs in galaxy mergers. They also show that the inclusion of BHs does not significantly modify the small difference in the SFH in SPH and AMR methods. This shows that the conclusions in this paper should be robust to the numerical treatment of hydrodynamics, in spite of recent concerns about the accuracy of the classical SPH formulation in certain situations (e.g. Agertz et al. 2007).

### 2.3 Semi-analytic models and Simulated Merger trees

In this paper we use the same approach as Moster et al. (2011) and MMS14, and refer to those papers for a more extensive discussion. In our method, presented schematically in Fig. 1, we build a dark matter tree from a large-scale  $N$ -body simulation and use the SAM of Somerville et al.

(2008) to populate the  $N$ -body merger tree with galaxies. The SAM predicts the baryonic properties for each galaxy within the halo merger tree by applying simple but physically motivated recipes for cooling and accretion, star formation and chemical enrichment, stellar feedback, black hole growth and AGN feedback, and morphological transformation and starbursts in mergers. The radial sizes of disks are modelled using an angular momentum based approach which has been shown to predict a size-mass relation that is in very good agreement with observations up to  $z \sim 2$  (Somerville et al. 2008). These SAMs have been extensively tested and shown to reproduce many fundamental statistical properties of galaxies, including stellar mass functions and luminosity functions from  $z \sim 0$ –6, disk gas fractions, and the fraction of different morphological types from  $z \sim 0$ –3 (Somerville et al. 2008, 2012; Porter et al. 2014; Brennan et al. 2015).

In Fig. 1 we show an example of such a merger tree, where time runs from top to bottom. At a chosen time  $t_i$  we extract a halo with its baryonic properties and merger tree. In this simple example the main system experiences four mergers, at  $t_1$ ,  $t_2$  (two) and  $t_3$ . At  $t_i$  we obtain the properties from the SAM, and create a particle realisation of the main halo ( $C_i$ ), represented by the brown arrow. In Fig. 1, this generated galaxy is shown in the top right, and consists of a dark matter halo (grey), a hot gaseous halo (red), a cold gaseous disc (blue), a stellar disc (yellow) and a stellar bulge (green). We then simulate the evolution of this galaxy up to  $t_1$ , at which point we add a particle realisation of satellite galaxy  $S_1$  to the simulations. While we obtain all baryonic properties from the SAM, the orbital parameters of  $S_1$  are directly taken from the dark matter  $N$ -body simulation. In this way we create a cosmologically motivated merger history.

After the inclusion of this satellite galaxy, we evolve the system in our simulations up to  $t_2$ . At  $t_2$  we add two more

satellites ( $S_2$  and  $S_3$ ) at the virial radius using the same method as before and continue the evolution of the system. We repeat this procedure up to the end of the simulation at  $t_f$ . By using this method we naturally include multiple mergers, such as at  $t_2$  and at  $t_3$  where one of the satellites is still orbiting when satellite  $S_4$  enters the halo. The growth of the main halo occurs through two channels. First, the main halo accretes gas and dark matter, which takes place from  $t_i$  to  $t_1$  or from  $t_3$  to  $t_f$  in the given example. Second, smaller satellite galaxies feed the main halo through mergers, e.g. from  $t_1$  to  $t_2$ .

### 2.3.1 Galaxy Initial conditions

We follow the description provided by Springel et al. (2005), with the extension of Moster et al. (2011) to create particle realisations for our initial conditions. Each galaxy consists of two stellar components (a disc and a bulge with masses  $M_{\text{disc}}$  and  $M_b$ ), two gaseous components (a cold disc and a hot halo with masses  $M_{\text{cg}}$  and  $M_{\text{hg}}$ ), and a dark matter halo with mass  $M_{\text{dm}}$ .

The stellar and gaseous discs are set up such that they are rotationally supported and have surface density profiles that decline exponentially outwards. The parameter  $\chi$  couples the scale length of the cold gaseous disc to that of the stellar disc by  $r_g = \chi r_d$ , and the vertical structure of the discs is determined by a radially independent  $\text{sech}^2$  profile with scale height  $z_0$ . The velocity dispersion in the stellar disc is set equal in the vertical and radial direction, while the gas temperature is determined by the equation of state (EOS). A balance of the pressure due to the EOS and the gravitational potential then determines the vertical structure of the disc selfconsistently.

For the stellar bulge and dark matter halo, we assume a Hernquist (1990) profile with scale lengths  $r_b$  and  $r_s$ . The dark matter halo is characterised by a concentration parameter  $c = r_{\text{vir}}/r_s$  and a halo spin  $\lambda$ . We assume that the stellar bulge is spherical and non-rotating.

Moster et al. (2011) calibrated the properties for a hot gaseous halo in order to match the cosmic star formation rate. We adopt a spherical slowly-rotating density profile, that follows the observationally motivated  $\beta$ -profile (e.g. Cavaliere & Fusco-Femiano 1976; Eke et al. 1998). Requiring that pressure supports an isotropic model and hydrostatic equilibrium within the gravitational potential fixes the temperature profile of the hot gaseous halo. A further calibration needed was the specific angular momentum of the gaseous halo, and we follow Moster et al. (2011) in setting the specific angular momentum of the gaseous halo  $j_{\text{hg}}$  to a multiple  $\alpha$  of the dark-matter specific angular momentum  $j_{\text{dm}}$ , such that  $j_{\text{hg}} = \alpha j_{\text{dm}}$ , with  $\alpha = 4$ .

In simulations with BHs, the initial mass of the BHs is extracted from the SAM, but due to resolution limitations we only include BHs with a mass larger than  $10^6 M_\odot$ . All the stellar and gaseous parameters (e.g.  $M_{\text{disc}}$ ,  $M_b$ ,  $M_{\text{cg}}$ ,  $M_{\text{hg}}$ ,  $r_d$ , etc.) are taken from the SAM predictions, while the dark matter parameters ( $M_{\text{dm}}$ ,  $c$ ,  $\lambda$ ) and all the orbital parameters (position and velocity) of the mergers are taken directly from the  $N$ -body simulation.

### 2.4 Merger tree selection

We set the lower mass limit of satellite galaxies to be included in the numerical realisation to 1/15 of the mass of the central galaxy. We chose this limit because it has been previously shown that mergers with a mass ratio  $\frac{M_{\text{host}}}{M_{\text{sat}}} > 5$  barely influence the SFR (Cox et al. 2008)<sup>1</sup>. Although we could therefore exclude any satellites with  $\frac{M_{\text{host}}}{M_{\text{sat}}} > 5$  from our simulations, we choose to be conservative and set the limit at  $\frac{M_{\text{host}}}{M_{\text{sat}}} = 15$ , in order to catch any possible secondary effects on the merger trees of slightly smaller satellites.

From the  $N$ -body+SAM simulation we selected 12 merger trees based on the following criteria:

- The final mass of the halo has to be of the same order of magnitude as that of the Milky Way (e.g.  $2 - 3 \times 10^{12} M_\odot$ )
- The merger tree must contain at least one major merger
- The total sample has to contain mergers of every mass ratio from 1 to 5 in steps of 0.5.
- The galaxy with the smallest mass ratio should enter the virial radius after redshift 1.5

Milky Way mass galaxies sit at the peak of SF efficiency (Fig. 2), and the transition between disc to spheroid dominated systems also occurs at this mass scale (Conselice 2006). Both of these effects are strongly related with mergers. In addition, the steep relation between halo and stellar mass at lower masses results in a drop of the influence of major stellar mass mergers for lower mass galaxies. At higher mass, it has been shown that additional feedback recipes are needed to prevent over-cooling (e.g. Vernaleo & Reynolds 2006; Gabor et al. 2011; Vogelsberger et al. 2014; Schaye et al. 2015).

We invoke the second and fourth criteria to satisfy the aims of our study, i.e. determine the effect of the merger ratio on the star formation history in cosmologically motivated mergers at  $z < 1.5$ . The third criterion ensures that we sample the full range of merger ratios.

The final merging process of the two most massive galaxies is not disturbed significantly by other galaxies in the majority of the trees, so during the final merger they are similar to binary mergers. However, we selected three merger trees that harbor multiple simultaneous mergers, in order to study the importance of three body interactions (e.g. Moreno 2012).

We also evolved the central galaxy in isolation for the same time interval, such that we have a control sample without mergers. We will refer to these simulations as the “isolated” cases. Each merger tree is simulated from a starting redshift  $z = 1.5$  down to  $z = 0$ . Finally we reran all merger trees with the addition of BHs and AGN feedback. All together we have a suite of nearly 100 different galaxies and simulations, leading to a substantial statistical sample.

## 3 STAR FORMATION EVOLUTION

We computed the stellar-to-halo-mass ratio for all of our initial and final central galaxies, and compared it to the

<sup>1</sup> We did run three merger trees with a cut of 1/50 to validate this assumption and found no substantial differences in the SF history.

Tree nr	$M_{\text{host}}$ $10^{10} M_{\odot}$	$M_{\text{sat}}$ $10^{10} M_{\odot}$	$\mu$	$M_{\star, \text{host}}$ $10^{10} M_{\odot}$	$M_{\star, \text{sat}}$ $10^{10} M_{\odot}$
661ws1	12.7	2.04	6.23	0.385	0.0895
661ws2	24.7	8.39	2.95	2.18	0.955
661bh1	13.9	2.11	6.59	0.313	0.226
661bh2	22.7	7.85	2.89	1.81	1.05
872ws	27.4	9.01	3.04	4.72	2.95
872bh	23.2	6.47	3.59	3.86	2.01
990ws	21.6	8.98	2.41	2.85	2.10
990bh	19.6	8.80	2.22	2.42	2.13
1166ws1a	3.21	0.77	4.17	0.781	0.104
1166ws1b	3.21	1.93	1.66	0.781	0.577
1166bh1a	3.46	1.05	3.30	0.650	0.132
1166bh1b	3.46	2.13	1.62	0.650	0.494
1178ws	7.42	2.66	2.79	0.700	0.452
1178bh	7.46	2.88	2.59	0.657	0.320
1188ws1	5.14	3.77	1.36	0.914	0.508
1188ws2	9.68	1.27	7.62	2.83	0.365
1188ws3	11.7	7.41	1.58	3.63	1.66
1188bh1	4.85	3.49	1.39	0.825	0.487
1188bh2	7.72	0.948	8.14	2.25	0.364
1188bh3	9.15	4.07	2.25	2.77	6.60
1415ws1a	1.04	1.19	0.87	0.197	0.221
1415ws1b	1.04	1.50	0.69	0.197	0.269
1415ws2	7.13	4.71	1.51	1.95	1.05
1684ws	10.8	5.33	2.02	2.78	0.605
1684bh	11.1	4.79	2.32	2.81	0.567
2096ws	4.49	3.95	1.14	0.728	0.373
2096bh	4.36	3.34	1.31	0.675	0.352
3747ws1	4.11	0.605	6.79	0.182	0.0414
3747ws2	3.97	2.82	1.41	1.39	0.366
3747bh1	3.72	0.856	4.35	0.167	0.106
3747bh2	3.83	2.34	1.64	1.28	0.199

**Table 2.** Properties of the progenitor galaxies immediately before they merge. Col. (1): the id number of the merger tree, (2) total mass of host galaxy within  $R_{\text{s,host}}$ , (3) total mass of satellite galaxy within  $R_{\text{s,sat}}$ , (4) merger ratio  $\mu = \frac{M_{\text{host}}}{M_{\text{sat}}}$ , (5) stellar mass of host within  $R_{\text{s,host}}$ , (6) stellar mass of satellite within  $R_{\text{s,sat}}$ . In Col. 1, the label *ws* means that the simulation was run with only the hot halo model, while the *bh* label means a simulation with hot halo and BHs. Numbers after these labels give the number of the merging event, and letters a subset of multiple merger events. Because merger trees 780 and 2809 do not have any mergers by  $z = 0$ , they are not included in this table.

constraints derived by Moster et al. (2013) using abundance matching. This comparison shows that the initial conditions and final properties of our galaxies are consistent with these constraints.

The results are shown in Fig. 2; although the initial conditions are mostly located within  $1\sigma$  of the relation, the galaxies at redshift  $z = 0$  mostly lie above the  $1\sigma$  region. This is not unexpected because we selected merger trees with active merger histories, which will have preferentially larger amounts of mass growth and SF than the average. Merger trees run with BHs do agree better with the stellar-halo mass relation, as feedback from AGNs reduces the SF. Overall our galaxies do not seem to suffer from a serious overcooling problem and are consistent with observations.

We simulated a total of twelve merger trees from redshift  $z = 1.5$  to  $z = 0$ , and summarise the characteristics of all mergers in Table 2. The merger ratio  $\mu = \frac{M_{\text{host}}}{M_{\text{sat}}}$  is an important parameter in this study. Satellite galaxies, after entering the halo of the central galaxy and before merging

with it, lose mass due to dynamical friction and ram pressure stripping (e.g. Boylan-Kolchin et al. 2008; Weinmann et al. 2012; Chang et al. 2013). This mass evolution introduces some arbitrariness in the definition of the merger ratio, because it depends on when it is computed. We decided to compute it right before the merger between the galaxies, in order to take into account the mass loss. We first fitted the dark matter profile of both galaxies, before the merger, to an NFW profile (Navarro et al. 1997) and obtained a value for the scale radius  $r_s$ . We then calculated the total mass (dark matter+gas+stars) inside  $r_s$  at the time of merging ( $t_1$ ) for both satellite and central, and used these masses to define  $\mu$ .

The mass ratios obtained with this method are in very good agreement with results from substructure finders like SUBFIND (Springel et al. 2001). This method was always able to distinguish between the central and satellite galaxies at very close encounters, whereas this proved difficult for SUBFIND.

### 3.1 The effect of the Hot Halo

As a first test, we compare simulated merger trees with and without the inclusion of the (observationally expected) hot gaseous halo component. We present the SFR for merger tree 990 in Fig 3, for a run without hot halo (left panel) and with hot halo (right panel). In each panel the results of the merger simulation are shown in red, while the isolated run (e.g. central galaxy without satellites) is shown in green. It is important to note that the merger ratio of two galaxies can vary after the removal of the hot halo, due to a different fraction of hot gas.

The cold-gas-only simulation is in agreement with previous studies (e.g. Cox et al. 2008); the SFR drops rapidly when the gas is depleted, and a starburst occurs during the final merging process. The starburst increases the SFR by an order of magnitude and there is almost no SF after the merger, because all the gas has been consumed during the starburst. The quenching of SF due to starvation is particularly clear in the isolated run, where we see a progressive fading of SF as time goes by. We caution that the relative increase in SF can be less than an order of a magnitude, for example, Di Matteo et al. (2007, 2008) find an average increase of a factor of  $\sim 3$  during mergers.

The simulation including a hot halo (right panel) shows a quite different behavior (as already noted by Moster et al. 2011). The hot halo cools and therefore the cold gas in the center of the galaxy is refuelled and SF can be sustained for the whole duration of the simulation; this is particularly clear in the isolated run.

Similar to MMS14, we see an important difference between the simulations with and without a hot halo during the merger. The starburst occurring in the simulation with a hot halo produces many more stars than the one in the simulations without a hot halo, however, the relative increase with respect to the isolated galaxies is smaller. In the simulations without a hot halo we observe an order of magnitude difference between the isolated and merging galaxies, which is significantly larger than the factor of  $\sim 6$  difference in the simulations with a hot halo. This difference is mostly due to the different evolution of the SFR in the isolated runs. The isolated galaxy without the hot halo depletes a large frac-

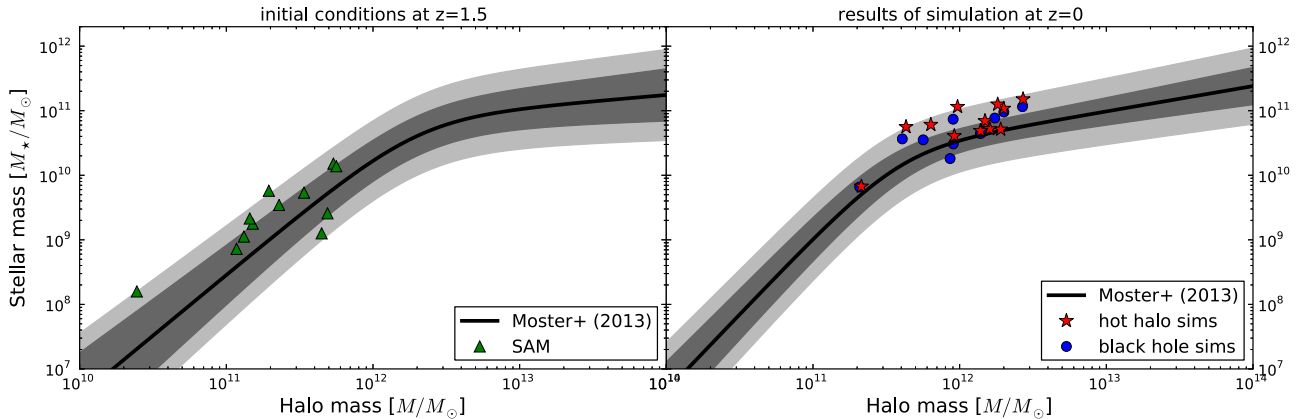


**Figure 2.** Stellar mass versus dark-matter mass within the virial radius. The left plot shows the initial galaxy properties obtained from the SAM, while the right plot shows the resulting simulated central galaxies at redshift zero. The red stars show the simulations with the hot halo model and the blue circles show the simulations with the hot halo model and BHs. Overplotted are the abundance matching constraints derived by Moster et al. (2013). The dark shaded area shows the  $1\sigma$  range on the constraints, and the light shaded area is the  $2\sigma$  range.

tion of its gas by forming stars in the first 2 Gyrs (before the merger happens), but when it has a hot halo surrounding it, it is able to keep forming stars for a longer period (because it replenishes its cold gas reservoir). This reduces the relative efficiency of a merger in triggering additional SF.

In Fig. 4 the SF History (SFH) of merger tree 780 is shown with and without the hot halo component. For the simulation without a hot halo, the behavior is very similar to tree 990, with an increased SF at  $t \sim 10$  Gyr. This “bump” in the SF clearly shows the effect of the merger, but it is not present in the simulation with a hot halo even though the mass ratio is very similar. When looking directly at the simulation snapshots at  $z = 0$ , we see indeed that the two galaxies did not merge and are at a distance of 73 kpc, despite two close passages (with distances of  $\sim 100$  kpc and  $< 5$  kpc) and in contrast to expectations based on the dark matter only simulation.<sup>2</sup>

Even more interesting is the *decrease* of SF in the merging hot halo simulation compared to the isolated galaxy. This decrease is seen over the full simulated period. This result is in contrast to the findings of previous merger simulations (e.g. Cox et al. 2008; Hopkins et al. 2009), where the SFR only experienced a positive boost due to interactions of galaxies. In order to better understand the origin of this SFR reduction we looked in more detail into the cold/hot gas fraction in the merger simulation.

Sinha & Holley-Bockelmann (2009) and Moster et al. (2011) already found that when two galaxies merge the hot halo component experiences heating due to the creation of shocks and the dissipation of the satellite galaxy orbital energy. This results in a net increase of the gas temperature and in a longer cooling time.

In Fig. 5 (bottom right panel) we show the temperature for the halo gas at a distance from 30 to 40 kpc from the galaxy center. This temperature is shown for the central

galaxy in isolation (green) during the merger (red) and for the incoming satellite galaxy again in isolation (blue) and in the merger simulation (cyan). For both galaxies (central and satellites) the gas temperature is higher in the merger run than in isolation, confirming the results of Moster et al. (2011). This higher gas temperature increases the cooling time, and reduces the amount of cold gas available for SF, as shown in the bottom left panel of Fig. 5. For the satellite galaxies the effects of ram pressure and tidal stripping make the difference between the isolated and merger cases even more pronounced. Finally the increased temperature of the hot gas and the subsequent reduced amount of cold gas decreases the SFR and produces a lower final stellar mass (right and left upper panels in Fig. 5) in the merger run with respect to the isolated case, making the merger an overall “inhibitor” for SF.

The increase of the SFR in the isolated host galaxy at  $\sim 6$  Gyr is caused by disk instabilities that originate from the accretion of cooling gas. Because the cooling rate is lower in the merger, the amount of accreted gas is insufficient to introduce the instabilities observed in the isolated case after 6 Gyr<sup>3</sup>.

Another important effect that might be at play in this galaxy is tidal stripping. If the first encounter at 4.8 Gyr generates strong tidal effects, a significant fraction of the cold gas can be expelled from the galaxies. This stripping would make the gas unavailable for star formation, and provides another method of reducing star formation that proposed above. However, when visually inspecting this galaxy, we find no signs of strong tidal effects, such as tails, during the first encounter. This shows that the difference in star formation between the isolated and merging galaxies is not dominated by tidal effects.

When looking at the complete suite of 12 merger trees, we see a number of important trends. First, in all simula-

<sup>2</sup> Since in this merger tree, and also in merger tree 2809, the two galaxies do not merge by  $z = 0$ , we did not use these merger trees in the remainder of the paper.

<sup>3</sup> The distance between the two galaxies increases from 200 kpc at 5.5 Gyr to 500 kpc at 7.5 Gyr, showing that during this period there is no significant interaction.



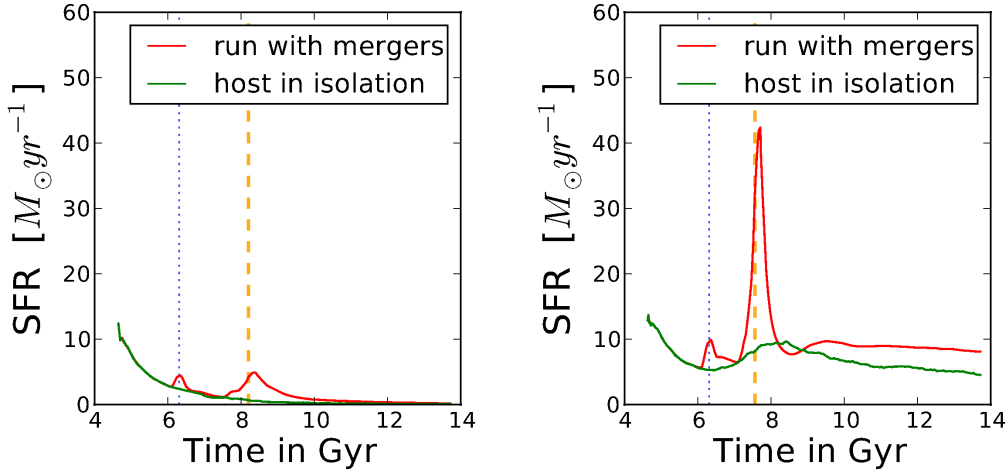


**Figure 3.** The SFR of merger tree 990. The left panel shows the simulations where no hot halo is present, and the right panel shows the simulations with a hot gaseous halo around the galaxy. The red line shows the SFR for the primary galaxy with the simulated merger, and the green line is the primary galaxy simulated in isolation. The vertical dashed orange line indicates the time when the merger occurs while the blue dotted line shows flyby's.

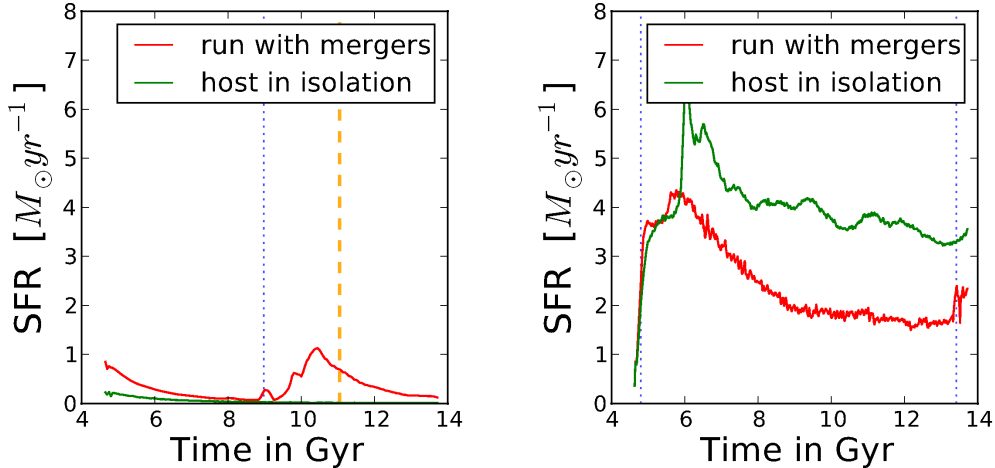


**Figure 4.** Same as Fig. 3 but for merger tree number 780.

tions the inclusion of the hot halo component increases the overall amount of SF both in the isolated runs and during mergers. The hot halo is able to refuel the cold gas reservoir and prevent the artificial quenching of SF due to gas depletion. Second, starbursts of varying sizes always occur during close encounters between galaxies. Mergers are able to funnel gas into the central region of the galaxy, where it is rapidly converted into stars. Most starbursts show a factor of  $\sim 6$  increase in SFR with respect to the isolated run of the same galaxy (see next section for a more quantitative results). Finally we found that mergers can also decrease the total SFR especially over long periods. Orbiting satellites increase the temperature of hot halo gas, by both the creation of shocks and transfer of orbital energy into thermal and kinetic energy of the gas through dynamical friction and hydrodynamic drag. The increased temperature of the hot

halo leads to longer cooling times, diminishing the amount of hot gas able to cool and reducing the overall amount of SF.

### 3.2 Starburst efficiency with hot halo

In MMS14 it was shown that star formation enhancement in multiple mergers can be significantly different than in a series of binary mergers. Here we extend the work of MMS14 on this issue. In this work we quantify our results in a more useful and descriptive way, so as to better compare the star formation during mergers in isolated binary mergers and in multiple mergers as predicted by cosmological merger trees. Following the approach of Cox et al. (2008) and Moster et al. (2011), we introduce the starburst efficiency parameter  $e_{\text{burst}}$ , defined as the fraction of cold gas



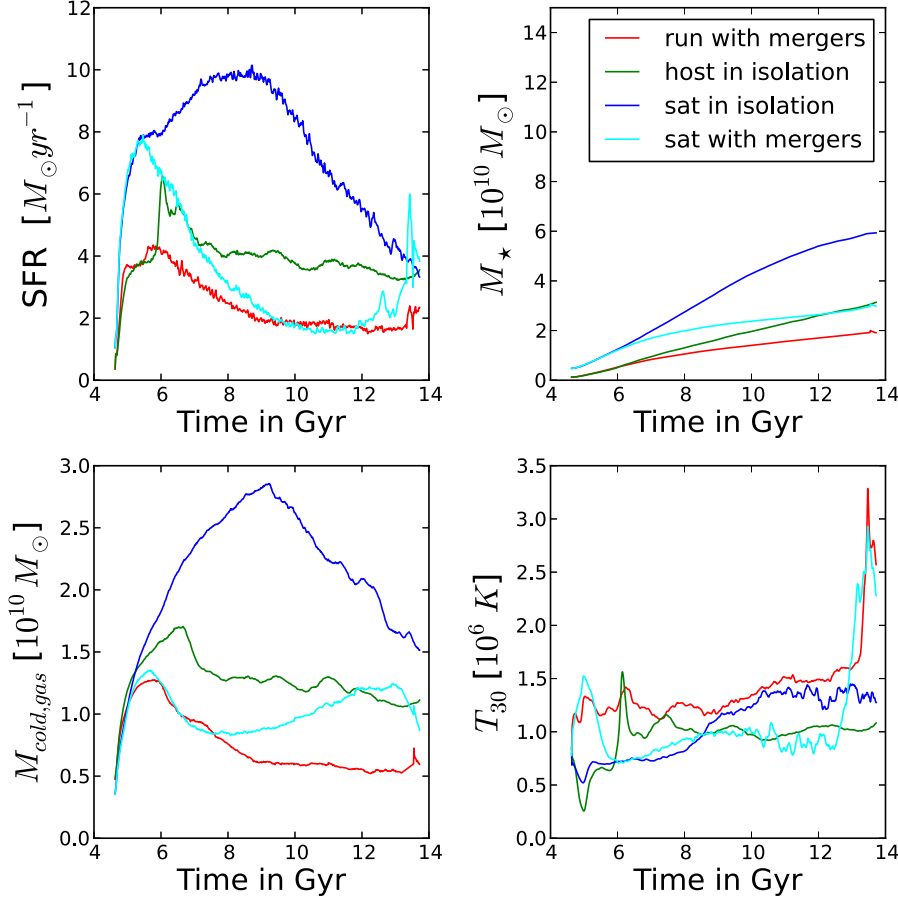


**Figure 5.** Merger tree 780: the top left plot shows the evolution of the SFR of this merger tree from redshift 1.5 to 0; the top right panel is the stellar mass over this period; the bottom left shows the amount of cold gas present in the galaxy, and the bottom right panel is the average temperature of the gas between 30 and 40 kpc around the galaxy. The red (green) line always shows the primary (secondary) galaxy in the merger simulation, while the blue (cyan) lines shows quantities for the primary (secondary) galaxy simulated in isolation.

present in the pre-merger galaxy that is consumed by the additional burst of SF.

$$e_{\text{burst}} = \frac{M_{\text{burst}}}{M_{\text{premerger, cold, gas}}}. \quad (1)$$

Where the burst mass  $M_{\text{burst}}$  is defined as the additional amount of stellar mass formed due to the merger between  $t_1$  and  $t_2$ , which defines the beginning and the end of the burst (e.g.  $t_1 = 7.5$  and  $t_2 = 8.5$  in the left panel of Fig. 3, and should not be confused with  $t_1$  and  $t_2$  from Fig. 1, which are the entry times of different satellites into the simulation):

$$M_{\text{burst}} = \int_{t_1}^{t_2} \text{SFR}(t) dt - \frac{1}{2} [\text{SFR}(t_1) + \text{SFR}(t_2)] (t_2 - t_1), \quad (2)$$

The burst masses and burst efficiencies from our suite of mergers are listed in Table 3. In addition, this table shows the bulge fraction  $f_{\text{bulge}}$ , the gas fraction  $f_{\text{gas}}$ , and other important properties of our mergers. The bulge fraction is calculated as described in detail by Kannan et al. (in prep.), but is based on a decomposition of the stellar component in a bulge and a disk, using the angular moment of the stellar particles, similarly to the approach of Scannapieco et al. (2011). Fig. 6 shows the relation between the burst efficiency and the galaxy merger ratio  $\mu$ . For  $\mu < 5$  there is a large

scatter in the values of  $e_{\text{burst}}$ , while for  $\mu > 5$  the starburst efficiency seems to converge to values around 0.15 (though the scatter is difficult to assess due to small number statistics).

Following Cox et al. (2008), we performed a power law fit to the burst efficiency as a function of mass ratio:

$$e_{\text{burst}} = e_{1:1} \left( \frac{M_{\text{sat}}}{M_{\text{host}}} \right)^\gamma. \quad (3)$$

We find that for our simulations including the hot halo the best fit is found for  $e_{1:1} = 0.52$  and  $\gamma = 0.81$ , and the resulting relation is shown in Fig. 6, along with the fit with the original values proposed by Cox et al. (2008, Eq. 5).

The values for  $e_{1:1}$  and  $\gamma$  are comparable to those found by Cox et al. (2008), but the large scatter in the  $e_{\text{burst}}$  values suggests that other parameters besides the mass ratio are impacting the burst efficiency. The larger scatter is due to three factors. First, the number of mergers included in this study is larger than in Cox et al. (2008), who fit to ten data points. Second, we use a range of cosmologically based orbits and initial galaxy properties, whereas Cox et al. (2008) only varied the mass ratio. Cox et al. (2008) show that the gas fraction, bulge-to-disk ratio and pericentric distance also influence the starburst efficiency, however, this is insufficient

Tree nr	$t_1$ Gyr	$t_2$ Gyr	$\mu$	$f_{\text{gas}}$	$f_{\text{bulge,host}}$	$f_{\text{bulge,sat}}$	$M_{\text{burst}}$ $10^{10} M_{\odot}$	$M_{\text{cold}}$ $10^{10} M_{\odot}$	$e_{\text{burst}}$
661	5.23	6.34	6.23	0.65	0.001	0.16	0.232	1.933	0.12
661	7.87	9.54	2.95	0.32	0.20	0.001	0.135	3.631	0.037
872	9.78	10.51	3.04	0.10	0.23	0.56	0.171	2.645	0.064
990	7.26	8.47	2.41	0.24	0.19	0.18	1.079	2.056	0.52
1166	7.60	8.30	4.17	0.50	0.22	0.33	0.123	1.161	0.11
1166	8.30	8.85	1.66	0.26	0.43	0.11	0.0365	1.444	0.025
1166 <sup>†</sup>	6.97	8.52	1.12	0.52	0.005	0.008	0.490	1.407	0.35
1178	7.80	9.80	2.79	0.52	0.047	0.18	0.538	2.854	0.19
1188	6.38	7.59	1.36	0.44	0.061	0.079	0.708	1.923	0.37
1188 <sup>†</sup>	6.41	7.36	1.52	0.44	0.10	0.10	0.736	1.430	0.51
1188	10.27	10.76	7.62	0.22	0.24	0.15	0.0617	1.141	0.054
1188	12.85	13.72	1.58	0.16	0.42	0.14	0.172	1.923	0.089
1415 <sup>††</sup>	7.70	8.85	0.87	0.55	0.26	0.08	0.671	1.139	0.59
1415 <sup>††</sup>	7.70	8.85	0.69	0.55	0.26	0.11	0.671	1.139	0.59
1415	11.65	13.00	1.51	0.18	0.45	0.10	0.458	0.804	0.57
1684	8.33	11.08	2.02	0.33	0.15	0.002	1.012	3.120	0.32
2096	7.81	10.03	1.14	0.44	0.055	0.024	2.125	2.838	0.75
3747	5.25	6.45	6.79	0.81	0.009	0.013	0.247	1.525	0.16
3747	9.95	11.40	1.41	0.37	0.21	0.20	0.813	3.058	0.27

**Table 3.** Results of the hot halo only simulations, where only ten out of the initial twelve merger trees contained major mergers. The first column gives the tree number, the second and third the begin and end of the starburst, the fourth the mass ratio from Table 2. In column five, six, and seven the cold-gas fraction within  $R_s$  of both galaxies, the bulge fraction of the host, and the bulge fraction of the satellite are given. The eighth column is the burst mass from equation 2, and the ninth is the amount of cold gas in the central region. The burst efficiency as defined in equation 1 is given in the last column. (<sup>†</sup>): The least massive of the three simultaneously interacting galaxies is removed and the merger is reran, see Sec. 4; (<sup>††</sup>): Combination of three galaxies, unable to distinguish contributions, so both merger ratios are given, see also Sec. 4.

to explain the large scatter. This is most clearly demonstrated by comparing merger trees 990 and 1178, which have similar properties, but significantly different burst efficiencies. Third and possibly most important, the more complex setting of the full merger tree influences the state of the galaxies.

In Fig. 7 we examine the origin of the scatter in more detail, and we show that the departure from the fitted power law cannot be explained by a single parameter. The scatter around the power law shows only weak trends with  $f_{\text{gas}}$ , or  $f_{\text{bulge}}$ . We use the duration of strong interaction,  $\Delta t$ , as a tracer of orbital influence, rather than trying to describe the orbit by an ellipse. If one did describe the orbit with an ellipse, the parameters of the ellipse would change between every time step due to interactions with other galaxies. Therefore, the initial orbital parameters are a very poor tracer of the final orbital parameters (see also Tsatsi et al. 2015). The final orbital parameters are better traced by  $\Delta t$ , where a more tangential orbit has a higher value of  $\Delta t$ . Although the overall distribution of the difference in burst efficiency seems random, there might be a trace of a positive trend with increasing  $\Delta t$  when we only select mergers with a similar merger ratio ( $1 < \mu < 2$ , large points in Fig. 7). The positive correlation between the duration of the encounter and the strength of the starburst was also found by Di Matteo et al. (2007). In summary, this shows that many factors contribute to the efficiency of the merger-triggered starburst and it may be difficult to devise a simple fitting formula. We will show in Sec. 5 that this conclusion holds after the addition of BH feedback to the simulations.

Tree	$t_1$ Gyr	$t_2$ Gyr	$\mu$	$M_{\text{burst}}$ $10^{10} M_{\odot}$	$M_{\text{cold}}$ $10^{10} M_{\odot}$	$e_{\text{burst}}$
780	9.35	11.65	1.03	0.111	0.340	0.328
872	11.00	12.60	2.99	0.008	0.341	0.023
990	7.55	9.70	2.43	0.187	1.066	0.176

**Table 4.** Results of the simulations without a hot halo. Only three out of twelve merger trees were simulated with these initial conditions. The columns correspond to columns 1, 2, 3, 4, 8, 9, and 10 from table 3.

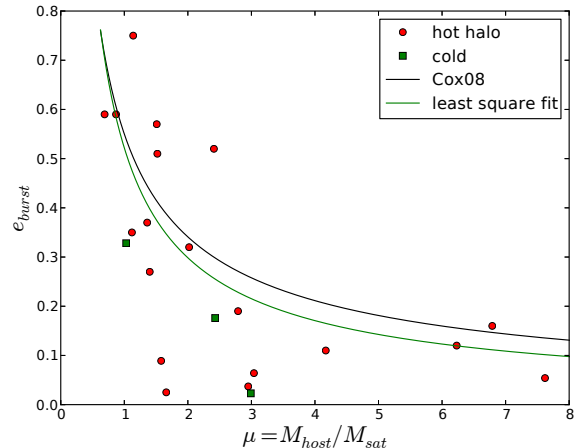


**Figure 6.** Mass ratio versus starburst efficiency. The red points are the mergers in the simulations with a hot halo, while the green squares show the simulations without a hot halo. The black line is the starburst efficiency relation of Cox et al. (2008) and the green line represents the least squares fit to our results.

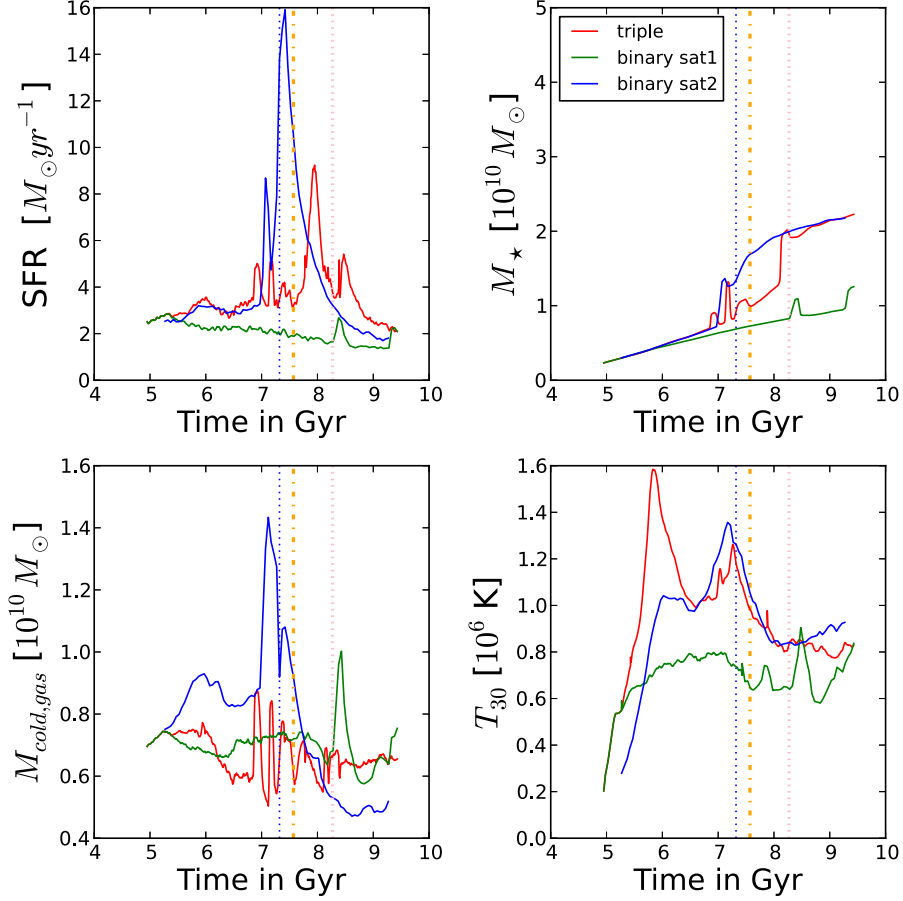


**Figure 8.** The multiple mergers in tree 1166. The top left plot shows the SFR, the top right plot the total stellar mass, and the bottom left plot the cold-gas mass in the central volume with radius of 20 kpc. The bottom right plot shows the average temperature of the halo gas between 30 and 40 kpc ( $T_{30}$ ). The red line is the central galaxy in the original simulation, and the green line shows the simulation where only the central galaxy and first satellite is included. The blue line shows the simulation where the first satellite is left out, and only the two most massive galaxies are included (the central galaxy and SAT2). The vertical orange dash-dotted line and pink dashed line indicate the time when the two satellites finally merge with the host galaxy ( $\mu = 4.17$  and  $\mu = 1.66$ ) in the simulation with a triple merger, while the vertical dotted blue line indicates the time when the galaxies merged in the binary merger simulation including only the most massive galaxies ( $\mu = 1.12$ ).

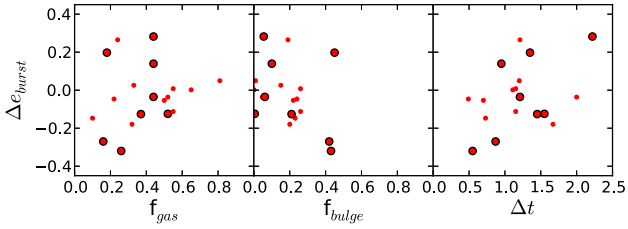


**Figure 7.** Difference between the burst efficiency compared to the power law fit to our results shown in Fig. 6,  $\Delta e_{\text{burst}} = e_{\text{burst}} - e_{\text{burst,PL}}$ . The difference is shown as a function of the gas fraction  $f_{\text{gas}}$ , the bulge fraction of the main galaxy  $f_{\text{bulge}}$ , and the duration of the starburst  $\Delta t = t_2 - t_1$ , which is a tracer of the orbital properties. The large circled points are all major mergers with  $1 < \mu < 2$ , while the smaller points are all more minor mergers.

## 4 MULTIPLE MERGERS

In addition to situations where only two galaxies interact simultaneously, so-called binary mergers, it also happens that more than two galaxies interact with each other or share a common halo. These multiple merger events are common in the LCDM universe (e.g., see Väisänen et al. 2008, for an observed merging triplet), and can have important consequences for galaxy evolution. In more than 50% of all merger pairs since  $z < 5$ , a second satellite enters the common halo within five dynamical times after the first satellite entrance (MMS14).

Nearly all previous studies on the effect of major mergers on SF focused only on binary mergers. Here we use our cosmologically motivated merger tree to study the effects of multiple strongly-interacting mergers on SF. We selected three merger trees (namely 1166, 1188, 1415) where at least three galaxies strongly interact with each other during a merger. We refer to these multiple strong interactions as multiple merger events.

In Fig. 8 we present the results for tree 1166. In each panel three different simulations are shown: 1) the multiple merger where the central galaxy first merges with the first satellite (SAT1) and then the second satellite (SAT2) enters the virial radius before the end of the first merger; 2) the binary merger between the central galaxy and the first satellite (without SAT2); 3) a binary merger between the central galaxy and SAT2, which happens to be more massive than SAT1.

The effect on SF is stronger in the merger of the two more massive galaxies (central and SAT2) than in the case of the triple merger. In the binary merger the starburst is more pronounced and more extended. The first satellite has a very minor impact on the SFR, moreover in the case of a triple merger SAT1 has an overall negative effect on the SFR, which is reduced with respect to the binary merger between central and SAT1.

Although the stellar mass formed in the starburst of the merger with only SAT2 is larger than in the original simulation, the stellar mass that resides in the galaxy at the end of both simulations is very similar. The difference in stellar mass formed is compensated by the accretion of the stellar mass native to SAT1, and therefore results in similar total stellar masses.

The reduced SF in the multiple merger is clearly due to the reduced amount of cold gas, as shown by the third panel in Fig. 8. In the multiple merger simulation the orbiting of the third galaxy increases the temperature of the hot gas (see the fourth panel of Fig. 8) delaying the cooling process. In Fig. 9 we show the distribution of gas in this merger tree at important stages of this interaction.

Fig. 10 shows the same panels as Fig. 8 for merger trees 1188 (upper row) and 1415 (lower row). In these plots we see similar results. In 1188 SAT1 is the most massive and indeed produces a larger starburst than the triple merger, in agreement to what we found in 1166. In merger tree 1415 we encountered a more complex situation. From Table 2 it can be seen that the merger ratio between the central galaxy and the two satellites SAT1 and SAT2 is less than 1 using our definition of  $\mu$ . This means that both the satellites are more massive than the central galaxy, and that the merger between the two satellites will be triggering the most SF, also in the triple merger. Simply replacing the central galaxy by one of the satellites and keeping the same orbital parameters, does not result in a merger before  $z = 0$ . The orbital parameters would therefore have to be significantly adjusted in order to have a merging binary system of the two satellites, and this would complicate the comparison. For all these reasons it is very difficult to compare the results of 1415 with the other multiple mergers.

## 5 EFFECT OF BLACK HOLE FEEDBACK

Feedback from accretion supermassive black holes can have an important effect in regulating SF during mergers (Di Matteo et al. 2005; Hopkins et al. 2006; Choi et al. 2012). During mergers, gas can be efficiently funnelled towards the center of the galaxy triggering rapid accretion onto the BH (Quasar phase) and a subsequent substantial deposition of energy into the interstellar medium.

To test this scenario we resimulated all our merger trees

with the addition of BHs and with our implementation of BH feedback (see Sec. 2.2). We also performed a simulation with BH but without the hot halo component for three merger trees, namely 780, 872, and 990. This is important to separate the effects of BHs and the hot halo and directly compare our results to previous studies. The top panels of Fig. 11 shows the results for merger tree 990 without the inclusion of the hot halo component. The upper left panel shows the SFR for three different simulations: host in isolation with BH, merger simulation with BH and merger simulation without BH. The SFR for tree 990 without a hot halo and without BH feedback is also shown for comparison (the same curve as shown in the left panel of Fig. 3). It is clear that the SFR rate is reduced in the presence of a BH, with the second peak lowered by more than a factor two.

The effect of the BH is even more clear in the lower left panel, where the mass of the cold gas is shown as a function of time. With the inclusion of BHs and associated feedback, the cold mass decreases and quickly becomes negligible. The decrease of the SFR and the cold-gas mass can be easily linked to the increase of the gas-accretion rate onto the BH (top right panel in Fig. 11). The accretion rate onto the BH is directly linked to the feedback energy output, responsible for heating the gas. These results are very similar to those of previous studies (e.g. Di Matteo et al. 2005; Springel et al. 2005; Hayward et al. 2014).

Next we included the presence of a hot gas halo in our initial conditions for merger 990 and reran it with BHs. The results are presented in the bottom row of Fig. 11. The simulation with BHs shows a similar trend as in the previous figure, when it is compared to the simulation without BHs but with hot halo. The total SFR is reduced and the second peak of SF (at 8 Gyr) drops by more than a factor 4. After the merger, SF is quenched to values as low as  $2 M_{\odot} \text{ yr}^{-1}$ , while without a BH the SFR was around  $10 M_{\odot} \text{ yr}^{-1}$ .

The inclusion of the hot halo has a strong influence on the later stage of the evolution of SF and cold-gas mass. After 10 Gyr the hot halo is able to substantially increase the cold-gas mass in the center of the halo through cooling, as is clearly shown in the top middle-left panel of Fig. 11. Thanks to this new cold gas reservoir, SF can increase again (contrary to the simulation with BH and no hot gas) and recovers to a SFR of several solar masses per year at the end of the simulation.

The higher cold-gas fraction in the run with the hot halo does not only increase the SF burst after eight Gyrs (with respect to a run without the hot halo) but also increases the accretion rate onto the BH as shown in the lower right panel in Fig. 11. This is true during the merger, but it is even more evident after ( $t > 9$  Gyrs), when there is a difference of more than one order of magnitude in the accretion rate of the simulation with and without the hot gas component. These higher  $\dot{m}_{bh}$  values result in a larger BH mass at the end of the run as shown in the bottom middle right panel of Fig. 11.

The effect of the BH on the gas distribution can be clearly seen in Fig. 12 where the surface density map of the gas in the merger 990 is shown. Before the merger ( $t=6$  and  $t=7$  Gyr) the BH is depleting the gas content in the center of the galaxy, while during the merger ( $t=8$  Gyr) a lot of gas is funnelled into the nucleus. This increases the accretion rate by about two orders of magnitude, releasing a lot of energy

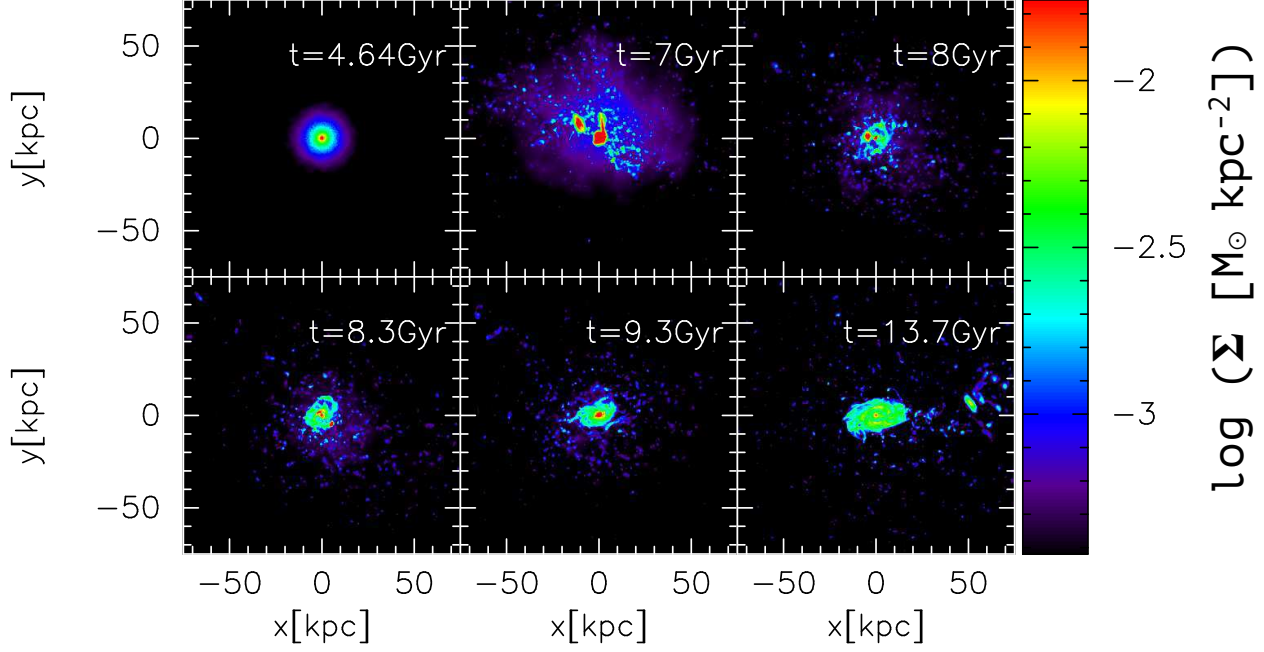


**Figure 9.** Distribution of gas in tree 1166. The different snapshots represent the start of the simulation ( $t=4.64$  Gyr), before, during, and after the multiple merger ( $t=7, 8, 8.3, 9.3$  Gyr), and the end of the simulation ( $t=13.7$  Gyr). Different colours correspond to different gas surface densities as shown in the key.

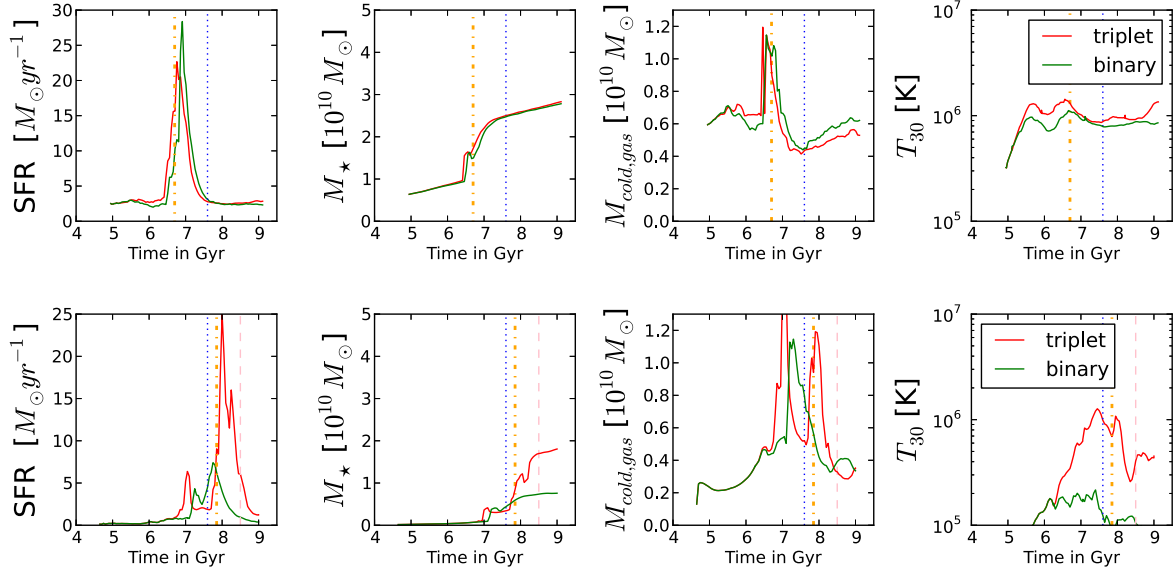


**Figure 10.** The multiple mergers in trees 1188 and 1415. The leftmost columns show the SFR, the second column the total stellar mass, and the third column the cold-gas mass within a radius of 20 kpc. The rightmost column shows the average temperature  $T_{30}$ . The red line is the central galaxy in the original simulation, and the green line shows the simulation where only the central galaxy and first satellite is included. The vertical orange dash-dotted and pink dashed lines (only in tree 1415) indicate the time when the two satellites merge with the host galaxy ( $\mu = 1.36$  for 1188, and  $\mu = 0.87$  and  $\mu = 0.69$  in the simulation with a triplet merger, while the vertical dotted blue line corresponds to the time when the galaxies merged in the binary merger where only the most massive galaxies are included in the simulation ( $\mu = 1.52$  for 1188, and  $\mu = 0.87$  for 1415).

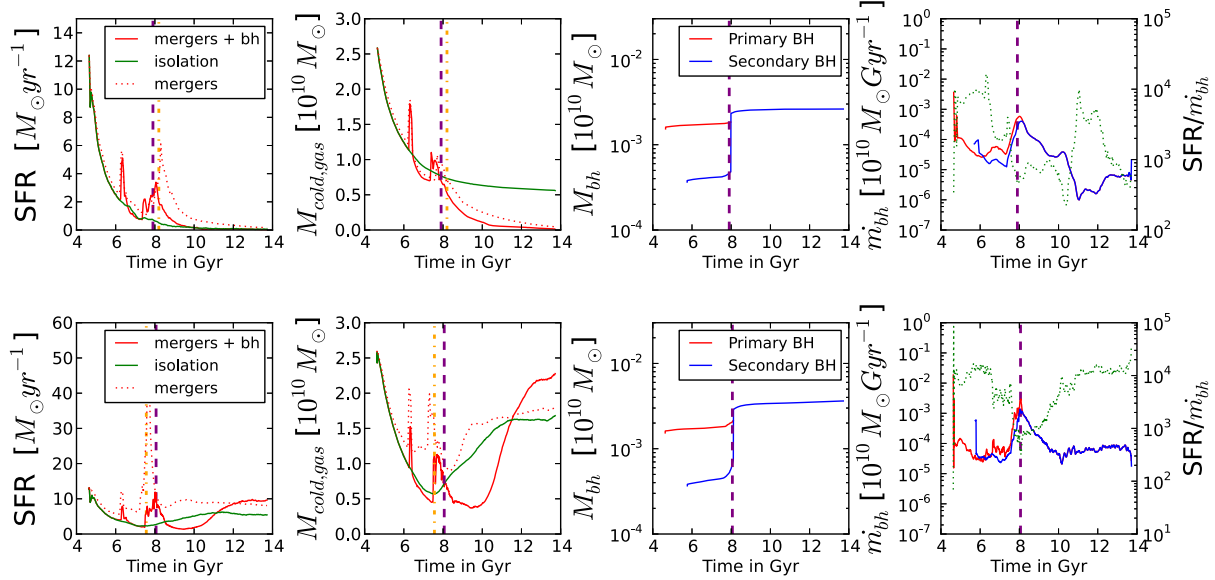


**Figure 11.** Merger tree 990 with BHs but without (top) and with a hot gaseous halo (bottom). For each row, the panels represent the following: in the left plots the SFR of the merger tree is shown, while the second plot from the left shows the mass of cold gas present in the galaxy. The right two panels show the BH mass and accretion rate. In the left two plots the solid red line shows the primary galaxy during the merging process, and the green line is the primary galaxy in isolation. Added to these plots are the results when BH feedback is not included, represented by the dotted red line. The red (blue) line in the right two plots shows the properties for the BH in the center of the primary (secondary) galaxy. When the galaxies and BHs merge the results for the merged BH continue as a single blue line. In the right plots we overplot a green dotted line, which corresponds to the ratio of SFR and  $\dot{m}_{bh}$  (merging galaxy), as indicated on the right vertical axis. The vertical lines in all panels indicate the time when the galaxies merge (orange dash-dotted for the simulation without BH, and vertical dashed purple for the simulation with a BH).

from the BH that again heats and depletes the gas in the central region ( $t=13.7$  Gyr).

The reduced SFR in the simulations including BHs brings the final galaxies (i.e. the merger products) into better agreement with the observed stellar-halo mass relation as already shown in Fig. 2, in agreement with previous studies that have shown AGN feedback is necessary to prevent the formation of overly massive galaxies, even at these mass scales (e.g. Somerville et al. 2008).

Let us now summarise the results of the whole ensemble of simulated trees with BHs. The mass of the BHs increases slightly during the first stage of the simulation, the pre-merger phase. Lower mass BHs grow relatively faster than larger BHs as a consequence of using the Bondi Hoyle accretion parametrisation.

The second growth phase is during the merger, when the accretion rate increases by an order of magnitude in most merger trees (see for example Fig. 11). We find a strong correlation between the presence and size of a starburst and the increase of the accretion rate of the BHs. Mergers that produce a large starburst also cause a large increase in the accretion rate, as both phenomena are related to the amount of cold gas in the galaxy center.

Most of the BHs merge within the simulation time (this is visible for example in the middle right panels of Fig. 11, where one line disappears at around 8 Gyrs). After the merger the accretion rate is quite low even in the presence of a hot halo component and the mass of the BH remains roughly constant.

These general trends are in good agreement with pre-

vious studies, e.g. Di Matteo et al. (2005), Springel et al. (2005), and Hayward et al. (2014), with the difference that in their simulations SF is quenched indefinitely because they do not include a hot halo, while in our simulations we find that after several gigayears the halo has cooled enough to provide fuel for SF.

The mass of the BHs at the end of the simulation can be compared to observations, for example using the correlation found between bulge mass and BH mass (e.g. Häring & Rix 2004; Sani et al. 2011; Kormendy & Ho 2013). In Fig. 13 we show that there is reasonable agreement between the simulated galaxies and observations. This is due to the self-regulated nature of the BH growth as shown in previous studies (e.g. Di Matteo et al. 2005).

In two simulations with BHs, namely those of merger trees 1166 and 1684, we see that the above described behaviour does not apply to every BH. In tree 1166, the third and smallest BH shows a fast and constant increase of its mass. In this merger tree there is an interaction between three galaxies and because of this, the third BH present in the smallest galaxy is able to move through the high-density gaseous medium of the other galaxies. This allows the BH to constantly accrete gas and keep increasing its mass, until it merges with the BH in the central galaxy. In tree 1684, the BH in the central galaxy shows barely any signatures of a merger and keeps increasing its mass exponentially throughout the entire simulation. This is probably due to the large amount of gas accreting onto the central galaxy.

Finally, similar to the previous section, we want to quantify the ability of mergers in triggering additional SF



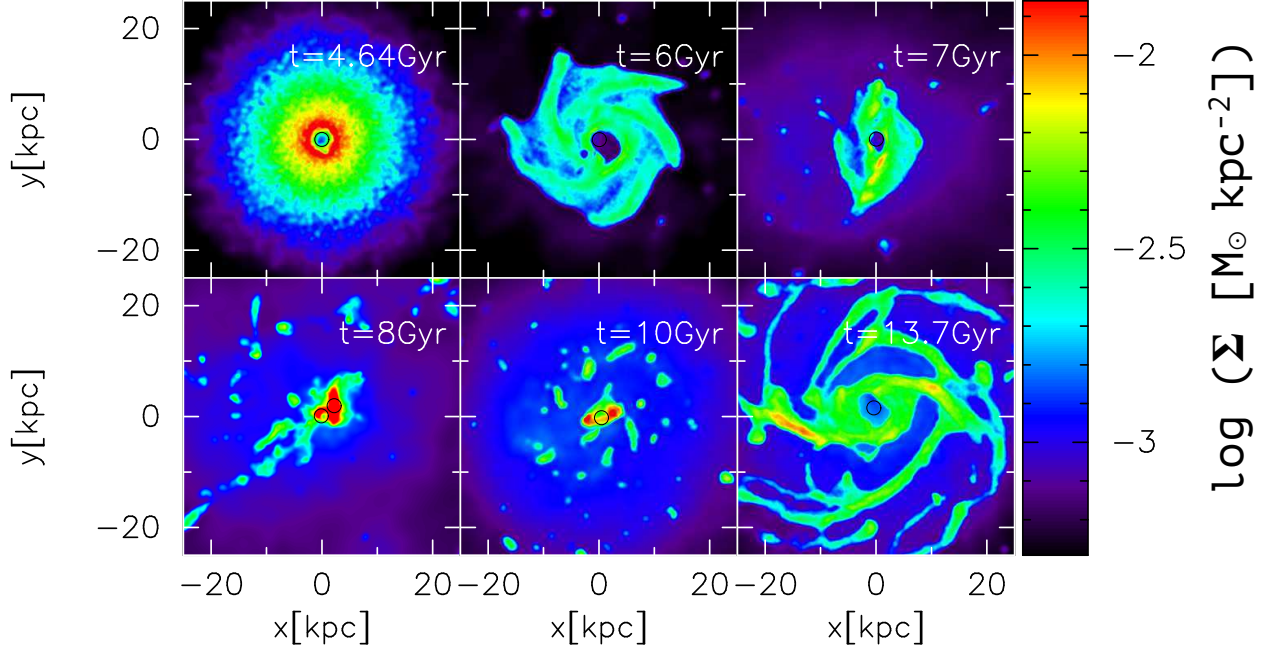


**Figure 12.** Gas surface density map of merger tree 990 with BH feedback included, shown at six different times. A depletion of gas can be seen around the BH (black empty circle) at all times, except during the merger at 8 Gyr, when more gas is transported into the nucleus of the galaxy, increasing the accretion rate of the BH.

Tree nr	$t_1$ Gyr	$t_2$ Gyr	$\mu$	$f_{\text{gas}}$	$f_{\text{bulge,host}}$	$f_{\text{bulge,sat}}$	$M_{\text{burst}}$ $10^{10} M_{\odot}$	$M_{\text{cold}}$ $10^{10} M_{\odot}$	$e_{\text{burst}}$
661	5.39	6.32	6.59	0.63	0.05	0.61	0.113	1.875	0.06
661	7.32	10.72	2.89	0.38	0.28	0.00	0.871	3.491	0.25
872	8.96	9.35	3.59	0.20	0.07	0.62	0.017	1.820	0.01
990	7.45	8.50	2.22	0.17	0.16	0.24	0.341	1.175	0.29
1166	7.18	8.89	3.30	0.43	0.05	0.01	0.184	1.329	0.14
1166	8.00	8.89	1.62	0.27	0.18	0.03	0.101	0.854	0.12
1178	7.40	9.75	2.59	0.50	0.02	0.24	0.666	2.174	0.31
1188	6.36	8.11	1.39	0.42	0.02	0.04	0.414	1.466	0.28
1188	10.27	10.52	8.14	0.11	0.85	0.02	0.002	0.508	0.004
1188	12.21	13.72	2.25	0.12	0.49	0.17	0.064	0.604	0.11
1684	8.45	8.90	2.32	0.31	0.11	0.00	0.028	2.384	0.01
2096	7.75	10.70	1.31	0.36	0.01	0.002	0.913	2.284	0.40
3747	5.20	6.25	4.35	0.79	0.01	0.00	0.285	1.566	0.18
3747	9.55	11.50	3.03	0.23	0.13	0.11	0.173	2.011	0.09

**Table 5.** Simulations with BHs, only nine out of twelve merger trees showed major mergers. See caption Table 3.

through the starburst parameter  $e_{\text{burst}}$ . The relation between the starburst efficiency and the merger ratio for simulations with BHs is shown in Fig. 14, while Table 5 is the analogue of Table 3 for these simulations.

It is clear from the figure that the inclusion of both the hot halo component and BHs strongly reduces the efficiency of massive major mergers in triggering additional SF with respect to previous studies (e.g Cox et al. 2008). Both the slope  $\gamma$  and the normalisation  $e_{1:1}$  of the power law are lower than found above, showing that the correlation between starburst efficiency and merger ratio is much weaker.

The weaker correlation between the merger ratio and the burst intensity could be partially due to a self-regulation mechanism between SF and BH feedback. A massive merger

is able to funnel a significant amount of cold gas towards the nucleus (e.g. Di Matteo et al. 2005); this cold gas provides fuel for the stellar burst but is also available to be accreted by the BH. While in the absence of a central BH a very massive merger will trigger a strong star formation episode (as shown in figure 6), in the presence of BH feedback the merger will also trigger accretion onto the black hole and the subsequent feedback, which will then suppress the stellar burst.

Finally, the large scatter in the relationship between burst efficiency and merger mass ratio suggests that other factors can have an important role in determining the strength of the starburst. In Fig. 15 we again investigate if there is a single parameter that controls this scatter, but



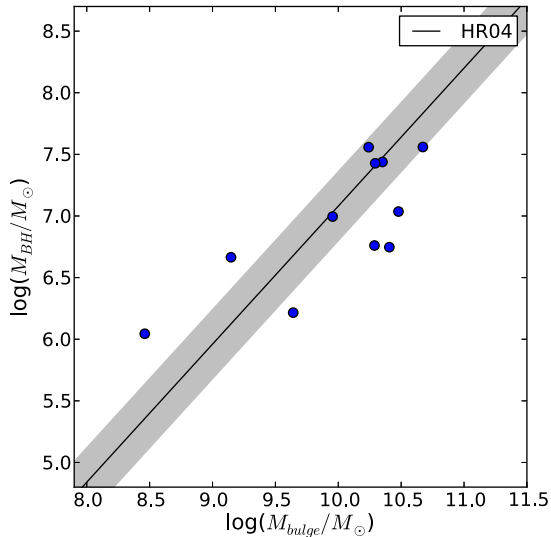


**Figure 13.** Bulge mass versus BH mass for the simulated galaxies at  $z = 0$  (blue points). The black line shows the observed correlation found by Häring & Rix (2004), while the grey area shows the intrinsic scatter in this relation.

Tree	$t_1$ Gyr	$t_2$ Gyr	$\mu$	$M_{\text{burst}}$ $10^{10} M_\odot$	$M_{\text{cold}}$ $10^{10} M_\odot$	$e_{\text{burst}}$
872	10.95	12.00	3.39	0.001	0.298	0.000
990	7.30	9.30	2.38	0.220	0.699	0.315

**Table 6.** Results of the simulations without a hot halo, but with a black hole. Only two out of twelve merger trees were simulated with these initial conditions. The columns correspond to columns 1, 2, 3, 4, 8, 9, and 10 from table 3.

we only find a possible weak trend with  $\Delta t$ , an indicator of the orbit. We plan to address the origin of this scatter in more detail in a future paper.

## 6 DISCUSSION

This study differs from previous ones in our method of obtaining initial conditions (IC) for numerical hydrodynamic merger simulations. Previous studies that included a hot gaseous halo (Cox et al. 2006; Moster et al. 2011; Choi et al. 2014) had ad hoc ICs, while here we adopted ICs that are cosmologically motivated. Therefore, the progenitors of our galaxies have a broad range of initial properties (gas fraction, morphology, size, etc.), and consequently, our results are more representative of an unbiased galaxy population.

Hayward et al. (2014) compared the performance of SPH to AREPO in merger simulations. They showed that SPH poorly resolves thermal instabilities, and it produces a significantly larger hot gaseous halo around galaxies than AREPO (Springel 2010), with spurious blobs of cold gas. The gravitational heating by satellites that we see in our simulations might be sensitive to these numerical issues, and should be more thoroughly tested with grid-based codes or improved versions of SPH. In addition, the blobs formed in SPH might spuriously contribute to the heating of the

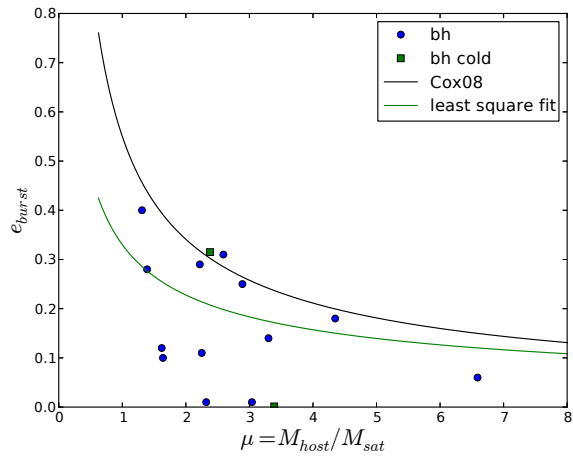


**Figure 14.** Merger mass ratio versus starburst efficiency. The blue points show all major merger events in simulations with a BH and a hot gaseous halo around the galaxy, while the green squares show the simulations with black holes and without a hot halo. The black line is the starburst efficiency of Cox et al. (2008) and the green line represents the least squares fit to our results.

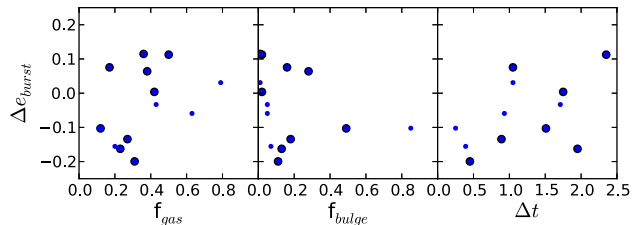


**Figure 15.** Difference between the burst efficiency compared to the power law fit to the data in Fig. 14,  $\Delta e_{\text{burst}} = e_{\text{burst}} - e_{\text{burst,PL}}$ . The difference is shown as a function of the gas fraction  $f_{\text{gas}}$  (left), the bulge fraction of the main galaxy  $f_{\text{bulge}}$  (middle), and the duration of the starburst  $\Delta t = t_2 - t_1$  which is a tracer of the orbit (right). The big circled points are all major mergers with  $1 < \mu < 3$ , while the smaller points are all mergers outside of this range.

hot halo, although it is likely a minor effect, as most of the heating occurs shortly before a merging event.

Although we find clear evidence that the recent merger history should be taken into account when calculating burst efficiencies, a full study of the effects of multiple mergers would require an additional substantial simulation effort, which is beyond the scope of this paper. We plan to address this in a forthcoming work.

In our suite of simulations, we find some significant starbursts for relatively large merger ratios ( $\mu > 5$ , see Fig. 6), contrary to what previous studies found. Because we focused on major mergers in this study, our selection criteria limit the number of minor mergers. Consequently, we do not have a large enough sample of minor mergers to constrain the dispersion in burst efficiency for minor mergers.

In Figs. 5 and 8, we see that the gas mass for the galaxies is nearly constant with time. Because the stellar mass does increase by a factor of  $\sim 2$  since  $z = 1$ , the gas fractions of these galaxies also decrease by a factor of 2. Since we

are looking at individual galaxies, it is difficult to compare the gas masses to observations. However, the trend that the gas fraction decreases by a factor of 2 over this period is compatible with observations (e.g. Santini et al. 2014). The constant cold gas masses are also in agreement with observations that the neutral-gas content of galaxies does not vary in galaxies that recently underwent a merger (Ellison et al. 2015).

From the stellar mass to halo mass comparison, we find that overcooling is not a major problem for the merger tree simulations discussed in this paper. However, this is in part due to the setup of our simulations, because they are based on SAMs that do include radio mode feedback. In addition, the rather large value of  $\alpha$ , the ratio of specific angular momentum of the hot halo gas and the dark matter, was calibrated to obtain galaxies with reasonable star formation histories (see Moster et al. 2011). For a test simulation with a significantly larger halo mass, we find very high SFRs caused by overcooling, indicating that at higher masses additional feedback such as radio mode AGN feedback is required (e.g. Somerville et al. 2008; Fanidakis et al. 2011).

We found, in agreement with previous studies, that the inclusion of AGN feedback reduces the efficiency of merger-triggered bursts. In our simulations, black hole accretion and the associated feedback are modelled in a relatively crude manner. Recent studies (e.g. Choi et al. 2014) have shown that the deposition of momentum from AGN-driven winds originating on the unresolved scales of the nucleus may have an even more dramatic effect, driving gas out of the nucleus in high-velocity outflows and further suppressing nuclear star formation.

## 7 CONCLUSIONS

Starbursts triggered by galaxy mergers have long been a topic of great interest in the literature. Here, we present important progress in the theoretical understanding of this phenomenon by improving on past studies in several ways. In particular, we employed the Simulated Merger Tree approach introduced in MMS14, in which cosmological merger trees combined with a semi-analytic model are used to obtain the initial conditions (orbit and galaxy properties) for a sequence of hydrodynamic merger simulations carried out with the SPH code GADGET2. As motivated by fully cosmological simulations and observations, but unlike most previous studies, our model galaxy-halo systems include a hot gaseous halo. We studied the impact of the inclusion of the hot gas halo, as well as that of BH feedback and multiple mergers, on triggered star formation enhancements in galaxy interactions, with a focus on major mergers.

Our main results can be summarised as follows:

- Owing to the presence of the physically and observationally motivated hot halo, our simulated galaxies are able to sustain SF for longer times, without experiencing artificial strangulation due to lack of cold gas.
- The starburst which results from the merger of two galaxies is relatively weak compared with most previous simulations. This is mostly because of the increase of the SFR at later times (due to the hot halo), which does not decrease the absolute size of the starburst, but does decrease its relative size.

- In some of our mergers the total SF is *decreased* with respect to the SF of the same galaxy run in isolation. This implies that mergers can also have a *negative* effect on SF. This decrease of SF is caused by the transfer of orbital energy of the merging galaxies into thermal and kinetic energy of the hot gas and by the generation of shocks in the hot halo during the merger. These heating processes increase the cooling time of the hot circumgalactic gas and lead to a lower SFR in the latest stage of the mergers. This also shows that extra heating terms are present during merging processes and should be taken into account in galaxy evolution models.

- We showed that three simultaneously merging galaxies should not be treated as two independent and consecutive mergers. The starburst resulting from a triple merger can be either similar to the one of the merger of the two most massive galaxies or can even be *smaller*. These results underline once more the complex dynamics of multiple mergers and the non-linear effect of different heating and cooling mechanisms.

- When we include thermal feedback from massive central BHs, we find that the efficiency of merger-triggered starbursts is reduced, especially right after the merger. Overall, BHs substantially reduced the stellar mass of the merger remnants, bringing them in better agreement with abundance matching predictions.

- Finally, following previous studies, we described the efficiency of mergers in triggering a starburst by a power-law function of the merger mass ratio. In absence of BHs, we find good agreement in the normalisation of this relation with Moster et al. (2011) who found  $e_{1:1} = 0.51$  in their hot halo simulation, while we find  $e_{1:1} = 0.52$  for a larger sample of galaxies. Our value for the index of the power-law  $\gamma = 0.81$  is in reasonable agreement with the value found by Cox et al. (2008) ( $\gamma = 0.69$ ). However, the scatter that we find is significantly increased, arguing against using a single fit to determine burst efficiencies for individual galaxies. When we include feedback from BHs there seems to be a weaker dependence of the starburst efficiency on the merger mass ratio.

There are still numerous improvements possible for our simulations. For example, we have a quite crude description of the thermal feedback from the central black hole and we did not include momentum deposition from nuclear scale winds (Choi et al. 2014) or any jet-like (e.g. Cielo et al. 2014) or radio feedback from the BH.

Nevertheless our results clearly show the importance of including all galaxy components (DM, stars, hot gas, cold gas, BH) when performing galaxy merger simulations, and of adopting cosmologically motivated merger histories and initial conditions. Our results may be useful for improving the treatment of merger-driven starbursts in semi-analytic models of galaxy formation.

## ACKNOWLEDGEMENTS

The authors thank the anonymous referee for his/her useful comments. The numerical simulations used in this work were performed on the THEO cluster of the Max-Planck-Institut für Astronomie at the Rechenzentrum in Garching. WK, AV, and RK acknowledge support from the

Sonderforschungsbereich SFB 881 “The Milky Way System” (subproject A1) of the German Research Foundation (DFG). AVM also acknowledges financial support to the DAGAL network from the People Programme (Marie Curie Actions) of the European Union Seventh Framework Programme FP7/2007-2013/ under REA grant agreement number PITN-GA-2011-289313. RSS acknowledges the generous support of the Downsborough family.

## REFERENCES

- Agertz O., Moore B., Stadel J., Potter D., Miniati F., Read J., Mayer L., Gawryszczak A., Kravtsov A., Nordlund Å., Pearce F., Quilis V., Rudd D., Springel V., Stone J., Tasker E., Teyssier R., Wadsley J., Walder R., 2007, *MNRAS*, 380, 963
- Anderson M. E., Bregman J. N., 2011, *ApJ*, 737, 22
- Anderson M. E., Bregman J. N., Dai X., 2013, *ApJ*, 762, 106
- Barton E. J., Geller M. J., Kenyon S. J., 2000, *ApJ*, 530, 660
- Barton Gillespie E., Geller M. J., Kenyon S. J., 2003, *ApJ*, 582, 668
- Bell E. F., Phleps S., Somerville R. S., Wolf C., Borch A., Meisenheimer K., 2006, *ApJ*, 652, 270
- Bergvall N., Laurikainen E., Aalto S., 2003, *A&A*, 405, 31
- Bessiere P. S., Tadhunter C. N., Ramos Almeida C., Villar Martín M., 2014, *MNRAS*, 438, 1839
- Bondi H., 1952, *MNRAS*, 112, 195
- Bondi H., Hoyle F., 1944, *MNRAS*, 104, 273
- Borne K. D., Bushouse H., Colina L., Lucas R. A., Baker A., Clements D., Lawrence A., Oliver S., Rowan-Robinson M., 1999, *ApSS*, 266, 137
- Borne K. D., Bushouse H., Lucas R. A., Colina L., 2000, *ApJL*, 529, L77
- Bower R. G., Benson A. J., Malbon R., Helly J. C., Frenk C. S., Baugh C. M., Cole S., Lacey C. G., 2006, *MNRAS*, 370, 645
- Boylan-Kolchin M., Ma C., Quataert E., 2008, *MNRAS*, 383, 93
- Brennan R., Pandya V., Somerville R. S., Barro G., Taylor E. N., Wuyts S., Bell E. F., Dekel A., Ferguson H. C., McIntosh D. H., Papovich C., Primack J., 2015, *ArXiv e-prints*
- Brook C. B., Kawata D., Gibson B. K., Freeman K. C., 2004, *ApJ*, 612, 894
- Brook C. B., Stinson G., Gibson B. K., Shen S., Macciò A. V., Obreja A., Wadsley J., Quinn T., 2014, *MNRAS*, 443, 3809
- Bushouse H. A., Borne K. D., Colina L., Lucas R. A., Rowan-Robinson M., Baker A. C., Clements D. L., Lawrence A., Oliver S., 2002, *ApJS*, 138, 1
- Cavaliere A., Fusco-Femiano R., 1976, *A&A*, 49, 137
- Chang J., Macciò A. V., Kang X., 2013, *MNRAS*, 431, 3533
- Choi E., Naab T., Ostriker J. P., Johansson P. H., Moster B. P., 2014, *MNRAS*, 442, 440
- Choi E., Ostriker J. P., Naab T., Johansson P. H., 2012, *ApJ*, 754, 125
- Cielo S., Antonuccio-Delogu V., Macciò A. V., Romeo A. D., Silk J., 2014, *MNRAS*, 439, 2903
- Comerford J. M., Gerke B. F., Newman J. A., Davis M., Yan R., Cooper M. C., Faber S. M., Koo D. C., Coil A. L., Rosario D. J., Dutton A. A., 2009, *ApJ*, 698, 956
- Comerford J. M., Greene J. E., 2014, *ApJ*, 789, 112
- Conselice C. J., 2006, *MNRAS*, 373, 1389
- Cox T. J., Dutta S. N., Di Matteo T., Hernquist L., Hopkins P. F., Robertson B., Springel V., 2006, *ApJ*, 650, 791
- Cox T. J., Jonsson P., Somerville R. S., Primack J. R., Dekel A., 2008, *MNRAS*, 384, 386
- Cox T. J., Primack J., Jonsson P., Somerville R. S., 2004, *ApJL*, 607, L87
- Croton D. J., et al., 2006, *MNRAS*, 365, 11
- De Lucia G., Blaizot J., 2007, *MNRAS*, 375, 2
- Dehnen W., 2001, *MNRAS*, 324, 273
- Di Matteo P., Bournaud F., Martig M., Combes F., Melchior A.-L., Semelin B., 2008, *A&A*, 492, 31
- Di Matteo P., Combes F., Melchior A.-L., Semelin B., 2007, *A&A*, 468, 61
- Di Matteo T., Springel V., Hernquist L., 2005, *Nature*, 433, 604
- Duplancic F., O’Mill A. L., Lambas D. G., Sodr   L., Alonso S., 2013, *MNRAS*, 433, 3547
- Eke V. R., Navarro J. F., Frenk C. S., 1998, *ApJ*, 503, 569
- Ellison S. L., Fertig D., Rosenberg J. L., Nair P., Simard L., Torrey P., Patton D. R., 2015, *MNRAS*, 448, 221
- Ellison S. L., Patton D. R., Simard L., McConnachie A. W., 2008, *AJ*, 135, 1877
- Fanidakis N., Baugh C. M., Benson A. J., Bower R. G., Cole S., Done C., Frenk C. S., 2011, *MNRAS*, 410, 53
- Gabor J. M., Dav   R., Oppenheimer B. D., Finlator K., 2011, *MNRAS*, 417, 2676
- Gingold R. A., Monaghan J. J., 1977, *MNRAS*, 181, 375
- Governato F., et al., 2009, *MNRAS*, 398, 312
- Gupta A., Mathur S., Krongold Y., Nicastro F., Galeazzi M., 2012, *ApJL*, 756, L8
- H  ring N., Rix H., 2004, *ApJL*, 604, L89
- Hayward C. C., Torrey P., Springel V., Hernquist L., Vogelsberger M., 2014, *MNRAS*, 442, 1992
- Hernquist L., 1990, *ApJ*, 356, 359
- Hernquist L., 1992, *ApJ*, 400, 460
- Hodges-Kluck E. J., Bregman J. N., 2013, *ApJ*, 762, 12
- Hopkins P. F., Cox T. J., Younger J. D., Hernquist L., 2009, *ApJ*, 691, 1168
- Hopkins P. F., Hernquist L., Cox T. J., Di Matteo T., Robertson B., Springel V., 2006, *ApJS*, 163, 1
- Hoyle F., Lyttleton R. A., 1939, *Proceedings of the Cambridge Philosophical Society*, 35, 405
- Hwang H. S., Elbaz D., Dickinson M., Charmandaris V., Daddi E., Le Borgne D., Buat V., Magdis G. E., Altieri B., Aussel H., Coia D., Dannerbauer H., Dasyra K., Kartaltepe J., Leiton R., Magnelli B., Popesso P., Valtchanov I., 2011, *A&A*, 535, A60
- Kauffmann G., White S. D. M., Guiderdoni B., 1993, *MNRAS*, 264, 201
- Kazantzidis S., Bullock J. S., Zentner A. R., Kravtsov A. V., Moustakas L. A., 2008, *ApJ*, 688, 254
- Kazantzidis S., Zentner A. R., Kravtsov A. V., Bullock J. S., Debattista V. P., 2009, *ApJ*, 700, 1896
- Kennicutt Jr. R. C., 1998, *ApJ*, 498, 541
- Kim J.-h., Wise J. H., Abel T., 2009, *ApJL*, 694, L123
- Knapen J. H., James P. A., 2009, *ApJ*, 698, 1437
- Kormendy J., Ho L. C., 2013, *ARA&A*, 51, 511

- Koss M., Mushotzky R., Treister E., Veilleux S., Vasudevan R., Trippe M., 2012, *ApJL*, 746, L22
- Lackner C. N., Cen R., Ostriker J. P., Joung M. R., 2012, *MNRAS*, 425, 641
- Larson R. B., Tinsley B. M., 1978, *ApJ*, 219, 46
- Lin L., Koo D. C., Weiner B. J., Chiueh T., Coil A. L., Lotz J., Conselice C. J., Willner S. P., Smith H. A., Guhathakurta P., Huang J.-S., Le Floch E., Noeske K. G., Willmer C. N. A., Cooper M. C., Phillips A. C., 2007, *ApJL*, 660, L51
- Lotz J. M., Jonsson P., Cox T. J., Croton D., Primack J. R., Somerville R. S., Stewart K., 2011, *ApJ*, 742, 103
- Lucy L. B., 1977, *AJ*, 82, 1013
- Mihos J. C., Hernquist L., 1996, *ApJ*, 464, 641
- Monaco P., Fontanot F., Taffoni G., 2007, *MNRAS*, 375, 1189
- Monaghan J. J., 1992, *ARA&A*, 30, 543
- Moreno J., 2012, *MNRAS*, 419, 411
- Moster B. P., Macciò A. V., Somerville R. S., 2014, *MNRAS*, 437, 1027
- Moster B. P., Macciò A. V., Somerville R. S., Johansson P. H., Naab T., 2010, *MNRAS*, 403, 1009
- Moster B. P., Macciò A. V., Somerville R. S., Naab T., Cox T. J., 2011, *MNRAS*, 415, 3750
- Moster B. P., Macciò A. V., Somerville R. S., Naab T., Cox T. J., 2012, *MNRAS*, 423, 2045
- Moster B. P., Naab T., White S. D. M., 2013, *MNRAS*, 428, 3121
- Navarro J. F., Frenk C. S., White S. D. M., 1997, *ApJ*, 490, 493
- Navarro-González J., Ricciardelli E., Quilis V., Vazdekis A., 2013, *MNRAS*, 436, 3507
- Nikolic B., Cullen H., Alexander P., 2004, *MNRAS*, 355, 874
- Oser L., Ostriker J. P., Naab T., Johansson P. H., Burkert A., 2010, *ApJ*, 725, 2312
- Patton D. R., Ellison S. L., Simard L., McConnachie A. W., Mendel J. T., 2011, *MNRAS*, 412, 591
- Porter L. A., Somerville R. S., Primack J. R., Johansson P. H., 2014, *MNRAS*, 444, 942
- Querejeta M., Eliche-Moral M. C., Tapia T., Borlaff A., Rodríguez-Pérez C., Zamorano J., Gallego J., 2015, *A&A*, 573, A78
- Quinn P. J., Hernquist L., Fullagar D. P., 1993, *ApJ*, 403, 74
- Robertson B., Bullock J. S., Cox T. J., Di Matteo T., Hernquist L., Springel V., Yoshida N., 2006, *ApJ*, 645, 986
- Rupke D. S. N., Veilleux S., 2013, *ApJ*, 768, 75
- Sanders D. B., Mirabel I. F., 1996, *ARA&A*, 34, 749
- Sanders D. B., Soifer B. T., Elias J. H., Madore B. F., Matthews K., Neugebauer G., Scoville N. Z., 1988, *ApJ*, 325, 74
- Sani E., Marconi A., Hunt L. K., Risaliti G., 2011, *MNRAS*, 413, 1479
- Santini P., Maiolino R., Magnelli B., Lutz D., Lamastra A., Li Causi G., Eales S., Andreani P., Berta S., Buat V., Cooray A., Cresci G., et al. 2014, *A&A*, 562, A30
- Scannapieco C., White S. D. M., Springel V., Tissera P. B., 2011, *MNRAS*, 417, 154
- Schaye J., Crain R. A., Bower R. G., Furlong M., Schaller M., Theuns T., Dalla Vecchia C., Frenk C. S., McCarthy I. G., Helly J. C., et al. 2015, *MNRAS*, 446, 521
- Shakura N. I., Sunyaev R. A., 1973, *A&A*, 24, 337
- Sinha M., Holley-Bockelmann K., 2009, *MNRAS*, 397, 190
- Smith J. D. T., Draine B. T., Dale E. A., 2007, *ApJ*, 656, 770
- Somerville R. S., et al., 2008, *ApJ*, 672, 776
- Somerville R. S., Gilmore R. C., Primack J. R., Domínguez A., 2012, *MNRAS*, 423, 1992
- Somerville R. S., Hopkins P. F., Cox T. J., Robertson B. E., Hernquist L., 2008, *MNRAS*, 391, 481
- Spergel D. N., et al., 2007, *ApJS*, 170, 377
- Springel V., 2005, *MNRAS*, 364, 1105
- Springel V., 2010, *MNRAS*, 401, 791
- Springel V., Di Matteo T., Hernquist L., 2005, *MNRAS*, 361, 776
- Springel V., Hernquist L., 2002, *MNRAS*, 333, 649
- Springel V., Hernquist L., 2003, *MNRAS*, 339, 289
- Springel V., White S. D. M., Tormen G., Kauffmann G., 2001, *MNRAS*, 328, 726
- Stewart K. R., Bullock J. S., Wechsler R. H., Maller A. H., Zentner A. R., 2008, *ApJ*, 683, 597
- Stinson G. S., Bailin J., Couchman H., Wadsley J., Shen S., Nickerson S., Brook C., Quinn T., 2010, *MNRAS*, 408, 812
- Stinson G. S., Brook C., Prochaska J. X., Hennawi J., Shen S., Wadsley J., Pontzen A., Couchman H. M. P., Quinn T., Macciò A. V., Gibson B. K., 2012, *MNRAS*, 425, 1270
- Toomre A., 1977, in B. M. Tinsley & R. B. Larson ed., *Evolution of Galaxies and Stellar Populations Mergers and Some Consequences*. p. 401
- Toomre A., Toomre J., 1972, *ApJ*, 178, 623
- Treister E., Schawinski K., Urry C. M., Simmons B. D., 2012, *ApJL*, 758, L39
- Tsatsi A., Macciò A. V., van de Ven G., Moster B. P., 2015, *ArXiv e-prints*
- Väisänen P., Mattila S., Kniazev A., Adamo A., Efsthathiou A., Farrah D., Johansson P. H., Östlin G., Buckley D. A. H., Burgh E. B., et al. 2008, *MNRAS*, 384, 886
- Vernaleo J. C., Reynolds C. S., 2006, *ApJ*, 645, 83
- Villalobos Á., Helmi A., 2008, *MNRAS*, 391, 1806
- Villalobos Á., Helmi A., 2009, *MNRAS*, 399, 166
- Vogelsberger M., Genel S., Springel V., Torrey P., Sijacki D., Xu D., Snyder G., Nelson D., Hernquist L., 2014, *MNRAS*, 444, 1518
- Walker I. R., Mihos J. C., Hernquist L., 1996, *ApJ*, 460, 121
- Weinmann S. M., Pasquali A., Oppenheimer B. D., Finlator K., Mendel J. T., Crain R. A., Macciò A. V., 2012, *MNRAS*, 426, 2797
- White S. D. M., Rees M. J., 1978, *MNRAS*, 183, 341
- Zolotov A., Willman B., Brooks A. M., Governato F., Hogg D. W., Shen S., Wadsley J., 2010, *ApJ*, 721, 738
- Zwicky F., 1956, *Ergebnisse der exakten Naturwissenschaften*, 29, 344

## APPENDIX A: NUMBER OF PARTICLES IN SIMULATIONS

Tree nr	type	# gas particles	# DM particles	# stellar disc particles	# stellar bulge particles
661	h	1571597	334836	15085	0
661	s1	138912	27898	2568	385
661	s2	742202	232175	76331	0
780	h	6280052	1349400	15564	16734
780	s1	5963875	1147249	120169	1574
872	h	1453482	410260	92684	6500
872	s1	682182	180190	29934	55610
990	h	871822	286404	59640	0
990	s1	560605	166434	52888	14282
1166	h	1627114	423707	43320	0
1166	s1	1506889	343997	42881	0
1166	s2	621554	147212	12450	2784
1178	h	1537422	399421	51773	0
1178	s1	603668	159475	30877	11323
1188	h	588450	170546	43075	0
1188	s1	538931	129737	19534	3246
1188	s2	202764	48912	9662	0
1188	s3	479564	150252	36526	0
1415	h	311220	106454	6221	0
1415	s1	649892	142452	916	0
1415	s2	868248	221719	38571	0
1415	s3	2218312	728668	299116	5864
1684	h	1790040	394454	21398	31260
1684	s1	794874	231646	62530	0
2096	h	1821984	451966	58799	0
2096	s1	2077989	532028	99427	0
2809	h	2415406	649315	47665	0
3747	h	1697765	412381	22361	0
3747	s1	405737	86786	5210	0
3747	s2	1344089	381888	47913	10937

**Table A1.** The number of particles used to generate galaxies in our merger trees. Central galaxies are labelled in the second column with *h*, while the satellites are represented by *s*.